Adapting the Sudden Landslide Identification Product (SLIP) and Detecting Real-Time Increased Precipitation (DRIP) algorithms to map and predict rainfall-triggered landslides in the West-Cameroons' highlands (Central-Africa)

ALFRED HOMERE NGANDAM MFONDOUM (ngandamh@yahoo.com)
Universite de Yaounde I https://orcid.org/0000-0001-5917-1275

Pauline Wokwenmendam Nguet
Institute of Mining and Geological Research

Jean Valery Mefire Mfondoum
Universite Toulouse 1 Capitole Toulouse School of Economics

Mesmin Tchindjang
Universite de Yaounde I

Sofia Hakdaoui
Universite Mohammed V de Rabat Faculte des Sciences

Ryan Cooper
University of Texas at Dallas Erik Jonsson School of Engineering and Computer Science

Paul Gérard Gbetkom
Aix-Marseille Universite - Campus Aix-en-Provence Schuman

Joseph Penaye
Institute of Mining and Geological Research

Ateba Bekoa
Institute of Mining and geological Research

Cyriel Moudioh
Institute of Mining and Geological Research

Methodology

Keywords: SLIP, DRIP, Landsat 8, geohazard, West-Cameroons' Highlands, rainfall-triggered Landslides, LHZ, prediction model

Posted Date: March 25th, 2020

DOI: https://doi.org/10.21203/rs.3.rs-19292/v1

Version of Record: A version of this preprint was published at Geoenvironmental Disasters on July 30th, 2021. See the published version at https://doi.org/10.1186/s40677-021-00189-9.

Adapting the Sudden Landslide Identification Product (SLIP) and Detecting Real-Time Increased Precipitation (DRIP) algorithms to map and predict rainfall-triggered landslides in the West-Cameroons' highlands (Central-Africa)

Alfred Homère Ngandam Mfondoum*[1,2], Pauline Wokwenmendam Nguet[3], Jean Valery Mefire Mfondoum[4], Mesmin Tchindjang[2], Sofia Hakdaoui [5], Ryan Cooper[6] , Paul Gérard Gbetkom[7], Joseph Penaye[3], Ateba Bekoa[3], Cyriel Moudioh[3]

Abstract

Background – The SLIP and DRIP algorithms recently developed correlate Landsat 8 images and local daily precipitation records to map and time rainfall-triggered landslides. In many areas recently affected by that geohazard in west-Cameroon's highlands, only the dry season images are available, while rainfall data are recorded on a monthly scale.

Methods – The SLIP algorithm is modified, integrating the inverse NDVI to assess the soil exposure, the Modified Normalized Multi-band Drought Index (MNMDI) combined with the hydrothermal index to assess soil moisture, and the slopes in degrees. They are converted into binned layers and overlaid to map the recent landslide. The DRIP algorithm is also modified, using the monthly rainfall rescaled to a daily window and the days of rainfall per month. Their probability density function (PDF) curves are superimposed and their intersection are used to propose set dichotomous variables before and after the 28 October 2019 landslide event, for a prediction model.

Results – The Landslide Hazard Zonation (LHZ) map of latest landslides is effective at *100%*, while the overall accuracy is *77.8%* when integrating the control point around the disaster area. Moreover, for 1948-2018 individual thresholds of $0.22 \leq PDF$, and 2019 threshold of $0.29 \leq PDF$ between June and October, the risk of rainfall-triggered landslide is *95%*, while the 'no-landslide' probabilities are between *98.95%* and *99.99%*.

Conclusions – Based on the SLIP and DRIP algorithms, the proposed methodology offers a new alternative in case of voids and gaps between data. Improvements and comparisons with others models are in perspective.

Keywords – SLIP, DRIP, Landsat 8, geohazard, West-Cameroons' Highlands, rainfall-triggered Landslides, LHZ, prediction model.

---

[1]StatsN'Maps, Private Consulting Firm, 550 East Bethany Drive, suite#111, Allen, Texas 75002, USA. * Correspondence : stats.n.maps.expertise@gmail.com
[2]Department of Geography, University of Yaoundé I, Cameroon. ngandamh@yahoo.com; mtchind@yahoo.fr
[3] Institute of Mining and Geological Research, PoBox 4110, Yaoundé, Cameroon. nguetpauline@yahoo.fr
[4]Department of Statistics and econometrics, University of Toulouse Capitol 1, France. valerymfondoum@gmail.com
[5]Earth Observation department, Geo-Biodiversity and Natural Patrimony Laboratory, Geophysics, Natural Patrimony and Green Chemistry Research Center, Scientific Institute, Mohamed V University, Rabat, Morocco. s.hakdaoui@gmail.com
[6] Erik Jonsson School of Engineering and Computer Science, University of Texas in Dallas, Texas 75080, USA. Rdc190001@utdallas.edu
[7] Department of Geography, University of Aix-Marseille, France. Paul-gerard.gbetkom@etu.univ-amu.fr

Introduction

Landslide refers to a sudden outward and downward gravitational mass wasting process of earth materials (rock, soils, artificial fill), triggered by variety of external factors or mechanisms (earthquakes, rainfall, reservoir impoundment, anthropogenic activities), but which do not requires a transportation medium (water, air or ice) (Varnes and IAEG, 1984; Brusden, 1984; Crozier, 1986; Hutchinson, 1988; Cruden, 1991 and Courture, 2011. The materials may move by falling, toppling, sliding, spreading, or flowing (UNISDR, 2017; USGS, 2004).

Landslides are natural events, but may turn into serious geohazards responsible for casualties and economical losses worldwide (Petley, 2012). These include loss of lives and damage to human settlements and natural structures, which present a significant constraint for the development of the zones affected. According to the International Disaster Database of the Centre for Research on the Epidemiology of Disasters (CRED) (EM-DAT), since 1900 some 130,000 persons have lost their lives because of landslides and flash floods; and the economic losses amounted to over US$ 50 billion. In the period from 2000 to 2014, the corresponding figures were around 26,000 deaths and US$ 40 billion in losses. The actual figures are, however, much higher (UNISDR, 2017). At least 90% of landslides losses can be avoided if the problem is recognized before the landslide events (Brabb, 1993). Therefore, the mitigation measures requires to identify existing landslides, and/or to predict of future events and endangered zones. However, Landslide inventories suffer from underreporting at both regional and global scales. Even in developed countries, the database of landslides events are usually far from complete (UNISDR, 2017). Significant gaps in available landslide information additionally contribute to the shortcomings of landslide inventories due to the lack of routine global monitoring or cataloging systems, such as those available for hurricanes and earthquakes (Kirschbaum et al. 2009). However, mapping landslide deformation and activity is fundamental for the assessment and reduction of landslide hazards and risks (Zhao and Lu, 2018).

Remote sensing data and the geographic information system (GIS) process are very powerful tools to study the prevailing causal factors and achieve that goal (Tofani et al., 2013). Their integration leads to a standard tool known as landslide susceptibility mapping used around the world by various researchers (Guzzetti et al., 1999; Van Westen et al., 1999). The susceptibility of a given area to landslides can be determined and depicted using hazard zonation (Lin et al., 2017). Recent advances identify two sets of methods for landslides hazard zonation (LHZ), i.e. heuristic (knowledge-based) and data driven (statistical) approaches (Pardeshi et al., 2013).

The heuristic or qualitative approach relies on the distribution (inventory) analysis through field survey mapping, historical records, satellite images and aerial photo interpretation (Varnes and IAEG, 1984; Cruden, 1991; Colombo et al., 2005; Guzzetti et al. 2005; Galli et al., 2008). Others researchers use decision-action processes and weighing models, including the analytical hierarchy process (AHP) and its different derivatives (Komac 2006; Ghosh et al. 2011; Kayastha et al. 2012; Wu et al., 2016; Meena et al., 2019). The statistical or quantitative approach include bivariate and multivariate modeling methods to minimize subjectivity (Kanungo et al., 2006). Amongst bivariate methods, weights of evidence model, weighted overlay method, frequency ratio approach, information value method and fuzzy logic method are used (Blahut et al. 2010) (Martha et al., 2013; Preuth, et al., 2010; Lee, 2005; Sarkar et al., 2006; Singh et al., 2011). Multivariate are specifically logistic regression analysis, discriminant analysis,

artificial neural network (ANN) method and probabilistic approach (Guzzetti et al., 2005, Wang and Sassa, 2005; Lee et al., 2008; Kanungo et al., 2009; Pradhan et Lee, 2009; Bui et al., 2012; Calvello et al., 2013).

The accuracies of susceptibility maps resulting from both qualitative and quantitative methods are affected by data resolution and availability. It can be assume that, the best approach should be built in a flexible perspective that integrative all data accessible. It is the intent of the present study.

The main objective of this paper is to map the rainfall-triggered landslides occurrence and susceptibility. A hybrid model is adapting the NASA's Sudden Landslide Identification Product (SLIP) and Detecting Real-Time Increased Precipitation (DRIP) approaches. It is a method originally qualitative, which uses open source data at less cost and consequently fits Cameroon's local scientific and economic conditions. So to notice, the developed approach is neither meant to substitute the standardized SLIP and DRIP algorithms, but to adjust the experimental processing as possible to a context of missing data, in both quality and quantity, by proposing way-outs for efficient results.

Description of the SLIP and DRIP methodology

NASA developers proposed the SLIP and DRIP methodology to automate rainfall-induced landslide identification in Nepal (Fayne et al., 2019). It is a two-sided approach, using satellite imagery data to identify the landslide extent and precipitation data to frame the timing the landslide event. The main entry is Landsat-8 imagery and the processing were performed in a cloud environment, based on a spectral band analysis and ancillary field data.

Sudden Landslide Identification Product (SLIP) algorithm takes advantage of spectral properties of vegetation, slope, land-cover type, and soil moisture in biweekly (16 days) time steps to identify new areas of bare-earth exposure that may represent landslide events. A percent red change for Landsat-8, band 4, is computed between the ten composed recent images before the landslide and the most recent images after the event. Areas with at least a 40% increase in red reflectance are considered bare-earth exposed to landslide according to this criteria.

To pursue, the soil moisture is assessed by using a Modified Normalized Multi-band Drought Index (MNMDI), inspired from Wang and Qu (2007), and adapted to Landsat 8 spectroscopy. The last step integrates a Digital Elevation Model's (DEM) slope. The slopes values are extracted in degrees, and 20º is considered as the basis.

On the other side, noticing that a predominant triggering mechanism for landslides is rainfall (Petley et al. 2005), the Detecting Real-Time Increased Precipitation (DRIP) model leverages NASA's Global Precipitation Measurement (GPM) was used. It provides precipitation data with a more precise temporal window of occurrence for each potential event (Fayne et al. 2019). The DRIP algorithm identify the likely timing/date of peak of precipitation triggering potential landslide events and corresponding to the SLIP detected areas in a window of 16 days. Windows of 24, 48 and 72 hours are used to obtain continuous rainfall data and integrate into the model.

Therefore, the purpose of these two algorithms has been the landslide identification and extreme precipitation monitoring by using python 3 as programming language.

Methodology

Landslide is a function of susceptibility (spatial propensity to landslide activity) and temporal frequency of landslide triggers, and its assessment may be done on local (individual slope), regional, national, continental or event global scale (UNISDR, 2017). Hence, there is a need for its hazard assessment at various spatial scales. This study was carried out on a regional scale.

Study area

The study was conducted on a subset of Cameroon's west-highlands (Fig.1.a), covering 393 035 hectares. This area belongs to the Cameroon Volcanic Line (CVL), one of the several segments of the African plate, oriented NE–SW (Elsheikh et al., 2014; Wokwenmendam, 2019). The altitudes are between 700m and 2400 m. It is a transition area between the Cameroon's rainy and dry areas. Consequently, the annual rainfall are 100mm to more than 3300mm in the southern part around the city of Bafoussam, and 20mm to more than 2400 mm when evolving to the northern part around Njimom. Twelve months average temperature is between 26º and 28º Celsius. The vegetation melt highland forest and sub-tropical savanna, depending on the rainfall and the sun exposition. The population is 1,720047 inhabitants, with a density of 124 inhabitants per squared kilometer.

Because of the altitude and the rough elevation (Fig.1.b,c,d), human activities and settlements such as agriculture or buildings mainly occupy slopes or shallows, exposing their selves to natural hazards. As recent events for instance, on the 4th and 5th September 2018, terrain cracking followed by blocks slides damaged dozens of houses in the city of Foumban (Penaye et al., 2018; Fig.2.a), causing the delocalization of hundreds of inhabitants. Recently, during the night of 27 to 28 October 2019, a long and huge rainfall of about 36 hours triggered a rotational to translational landslide in Bafoussam (Kankeu & Ntchantcho, 2019; Fig.2.b), the deadliest in that area with 45 bodies found, dozens of unfounded people and at least 100 houses destroyed. This context justified the carry out of the present research, to help administrators anticipating such events and planning mitigation actions.

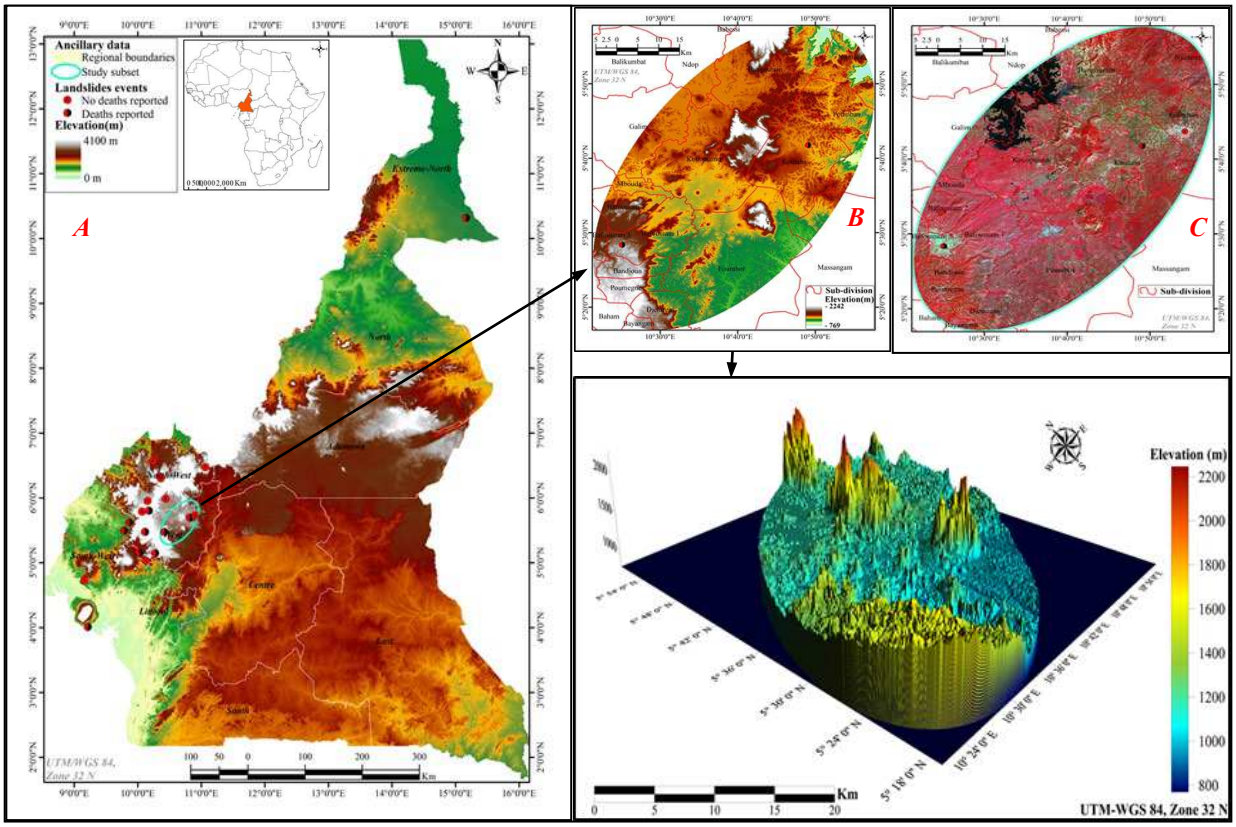

Fig.1. The study location. *A) Country elevation and landslides events. B) & C) – Subset of study elevation and Landsat OLI-TIRS image. D) 3-dimensional appraisal of the subset elevation.*

Fig.2. Scarps leaved by the landslides of Foumban (2018-*A*) and Bafoussam (2019-*B*). *Both events were sudden with transitional to rotational movements, but the one in Foumban happened in one-step, while the one in Bafoussam happened during at least two steps (yellow dashed), justifying three main blocks/stairs*.

Data acquisition and pre-processing

The experiment was conducted in a desktop script environment, using recent licensed versions of Erdas imagine, ArcGISPro and Xlstat software script environments. The main entry is the landsat-8 imagery, given the fact that multispectral image analysis is a popular technique in landslide detection (Martha et al. 2016). Taking the landslide of the 28 October 2019 as reference, twelve Landsat-8 images were downloaded from the United States Geological Survey website, distributed as eleven before the event and one after. Unfortunately, the cloud cover for the rainy season images are very important to stay in a16 days window for processing, so that the best images are available between December and March with at least two images per year. Freely available Landsat images are all Level-1 products, delivered as digital numbers (DNs). The bands used are 2-7, i.e. blue to SWIR2 (Table) with a 30 meters spatial resolution, and the panchromatic band is used to rescale the spatial resolution to 15 meters. Applying the Cosine Solar TAUZ (COST) radiometric calibration model of Chavez (1996) to the stacked image, blue-SWIR2, the DNs were converted from at-sensor radiance to top-of-atmosphere (TOA) reflectance via solar correction, and rescaled from 64-bit to unsigned 8-bit. Therefore, to precise, atmospheric corrections and haze reduction have helped to remove other noises and then approximate values of surface reflectance. The last step concerned the topographic correction that had addressed altitude artifacts.

The Shuttle Radar Topography Mission (SRTM) and the Advanced Spaceborne Thermal Emission and Reflection Radiometer (ASTER) Digital Elevation Models (DEMs) are also used. They are downloaded from the USGS and the NASA websites and they are integrated in the model to assess the slopes threshold for landslides triggering, while eliminating errors of commission in the processing (Jiménez-Perálvarez et al. 2011).

Another entry concerns the precipitation data. These data were combined from three main sources. The Tropical Rainfall Measuring Mission (TRMM) (Braun, 2011), Tropical Applications of Meteorology using Satellite data (TAMSAT) (Maidment et al., 2014) and some local meteorology services.

Image classification and NDVI computation for LULC extent assessment

All the cloud-free satellite images of the study area are only available for the dry season. There is a need of matching the land use land cover (LULC) with the rainy season when sudden landslides have always taken place. Then, an image of the rainy season was downloaded from 23 June 2019, and a cloud-free subset was extracted on the natural land covers area, i.e. vegetation and soil, and a supervised classification was performed for each image

(Fig.3.) Their average overall accuracy is *92%* and the average kappa coefficient is *0.89*. An image difference was then performed with the newest image (dry season) classification of the same year. The relation is expressed as follows:

$$\mathbf{Va = DRYsv + (RAINYsv - DRYsv)}$$

Where *Va* is the new vegetation area and *sv* is the season vegetation. It was noticed that in June, the 337 845 hectares of the classification subset were occupied by the vegetation up to 61% (205295 ha) versus *39%* (132550 ha) for soils, while in December, these percentages switch to 46% (155260 ha) for vegetation and *54%* (182587 ha) for soils (Fig.4.). To confirm the objects extraction and the trends above, the Normalized Difference Vegetation Index (NDVI) was computed for the two images (Fig.3.). The statistics gave (Figure 4.) *69%* (233113 ha) for vegetation and *31%* (104732 ha) for soil in June, versus *47%* (158787 ha) for vegetation and *53%* (179058 ha) for soil in December (Fig.4.). The average percentages are *65 %* for vegetation and *35%* for soils in June, versus 46.5% for vegetation and *53.5%* for soils in December. The ratios of the rainy season over the dry season areas were computed, showing that the rainy season vegetation area is about ***1.4*** times bigger than in dry season. Further, assuming that the average percentages could have the same influence on the classification process, the ratio of vegetation extent (*65%*) over the classification accuracy (*92%*) was calculated. The result obtained, i.e. ***0.598≈0.6***, was summed with the previous value, *1.4*, as the best vegetation extent approximation for the rainy season, i.e. *2* times the vegetation area of the dry season's the images used in the study. The ArcGISPro software expand function tool is useful for this purpose. In its principle, the class value targeted is multiplied by an *x* factor (*2* here) to approximate the area as needed. The algorithm is written as follows:

$$\mathbf{Out\_raster = Expand\ (in\_raster, number\_cells, zone\_values)}$$

With *in_raster* representing the reclassified raster image*, number_cells* being the *x* factor and *zone_values* standing for the class to be expanded.

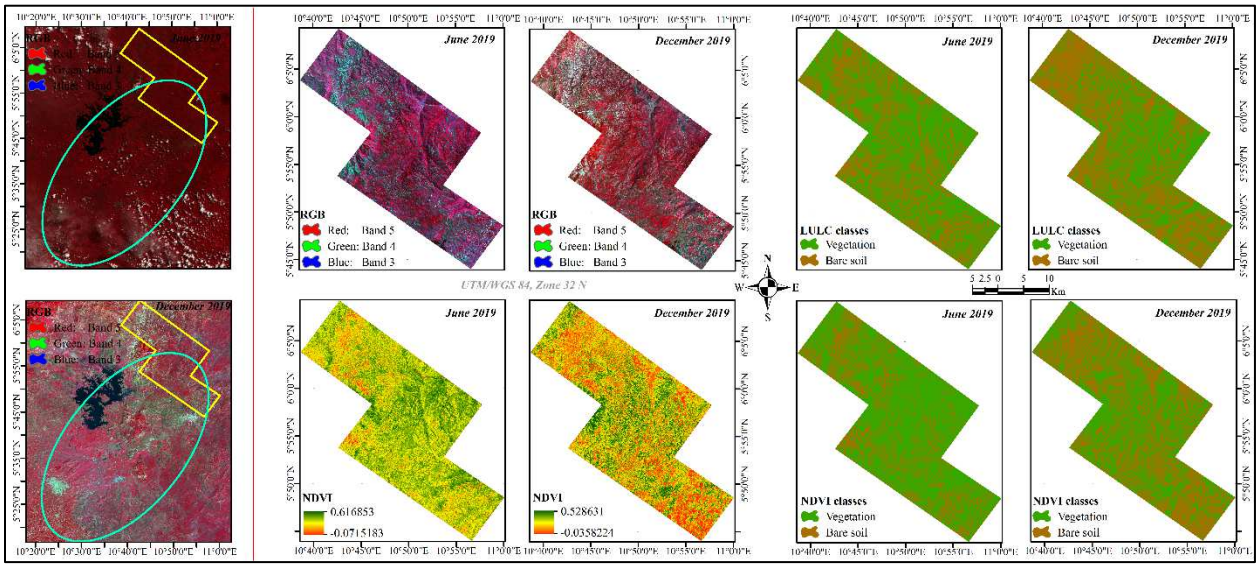

Fig.3. Subset of Landsat 8 images used for Land cover extent approximation

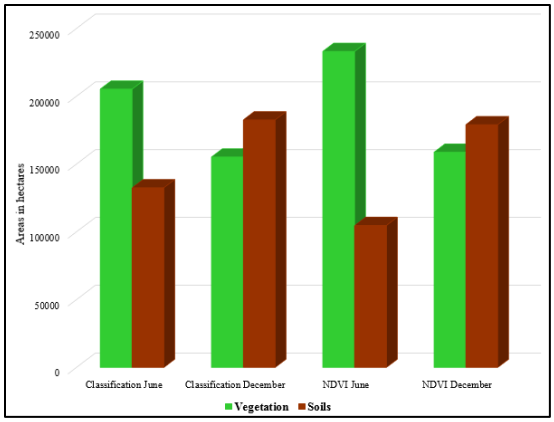

Fig.4. Land Use Land Cover (LULC) – comparison for the classification and the NDVI

Adapted SLIP algorithm

The first step is defining the soil exposure, i.e. the percentage of non-vegetated land. Fayne et al. (2019) proposed it as a rate of change in the red band reflectance between the current image before the landslide and a composed image of the ten red bands of the images before the landslide. The formula is expressed as follows:

$$\%\mathbf{Red}_{\mathbf{change}} = \left(\frac{\mathbf{Red}_{\mathbf{current}} - \mathbf{Red}_{\mathbf{composite}}}{\mathbf{Red}_{\mathbf{composite}}}\right) * \mathbf{100}$$

The images should be collected for consecutives months. In the present study, regarding the gap of almost ten months in the same year between two Landsat 8 usable images, the percentage formula described above was leading to infinite values. Then the red difference was modified to an Inverse Normalized Difference Vegetation Index, INDVI, to assess the non-vegetated land. The INDVI is proposed as the spectral difference between the red and the NIR wavelength, as follow:

$$\mathbf{INDVI} = \frac{\mathbf{Red} - \mathbf{NIR}}{\mathbf{Red} - \mathbf{NIR}}$$

After an average of the INDVI was computed for the ten oldest images, referring to the landslide of the 28 October 2019 in Bafoussam. Then, the average INDVI was subtracted from December's 2019 INDVI and the resulting image was normalized in percentage values, as follows:

$$\mathbf{INDVIn} = \frac{\mathbf{INDVI} - \mathbf{INDVImin}}{\mathbf{INDVImax} - \mathbf{INDVImin}} * \mathbf{100}$$

Where INDVIn stands for the normalized INDVI image, min and max are the minimum and the maximum of the INDVI. Values starting at *40%* were selected as indicators for soil exposure as proposed by Fayne et al. (2019). A binned image was then created, with *0* for vegetated areas and *1* for non-vegetated areas. Then, the vegetated class was expanded times *3* to approximate the land surface coverage in the rainy season, according to the classification statistics.

Further, the moisture was assessed by using two indices. The Modified Normalized Multi-band Drought Index (MNMDI) (Fayne et al., 2019) was computed between the near infrared (NIR) and the shortwave infrared (SWIR2) bands:

$$\mathbf{MNMDI} = \frac{\mathbf{NIR} - \mathbf{SWIR2}}{\mathbf{NIR} + \mathbf{SWIR2}}$$

To confirm and reinforce the soil moisture information, the hydrothermal index was computed. This index helps enhancing soils, rocks and minerals, as well as vegetation cover at a regional scale, based on a multiple ratios approach computation between the visible and infrared wavelengths (Pour, 2014). Band ratios concerned are 4/2, 6/7, 5 and 10 in red–green–blue), and the result is a three principal component analysis image. A linear regression was performed between each component and the MNMDI image, showing that the third component was positively correlated to MNMDI with the highest determination coefficient (R^2) up to *82%* (Appendix 1.). This band and the MNMDI images are stretched in the intervals [*0–11*] and [*-1.205 – 0.915*] respectively. The sum of the two images gave a new one stretched in the interval [*-1.205 – 11*]. Therefore, taking in account the moisture thresholds of [*-0.08 – 0.915*] for MNMDI and [*1.5 – 11*] for hydrothermal, a binned image was created between [*-0.08 – 11*], with *0* for no humidity and *0.75* for moisture.

The slopes values were computed based on the DEM-SRTM. The threshold fixed as enough to trigger landslide is *20°*. Slope intervals categories are *gentle* (*0°–20°*), *fairly steep* (*20°–35°*), *steep* (*35°–45°*), *very steep* (*45°–60°*), and *extremely steep* (*60°–90°*). A binned image was created with *0* for slopes less than 20° and *0.5* for slopes at or above 20°. The three conditioned layers binned values are recorded in table 1.

Table 1. SLIP conditioned layers

Layers	**Conditions for LHZ**	
	Excluded	*Included*
Uncovered soil	**0**	**1**
Soil moisture	**0**	**0.75**
Slopes	**0**	**0.5**

The three layers were submitted to a simple weight linear combination (SWLC) to map the areas were sudden landslides conditions are met. The overall SLIP process are described in fig. 5 and the layers are illustrated in fig.6.

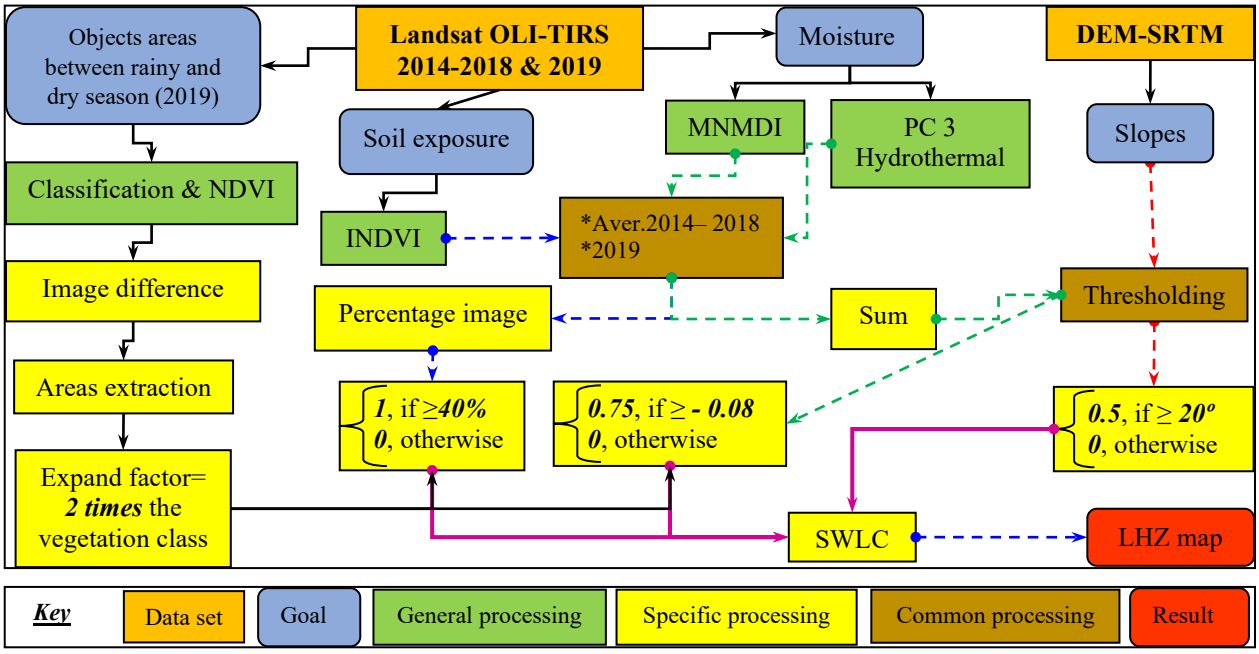

Fig.5. Workflow of the SLIP process

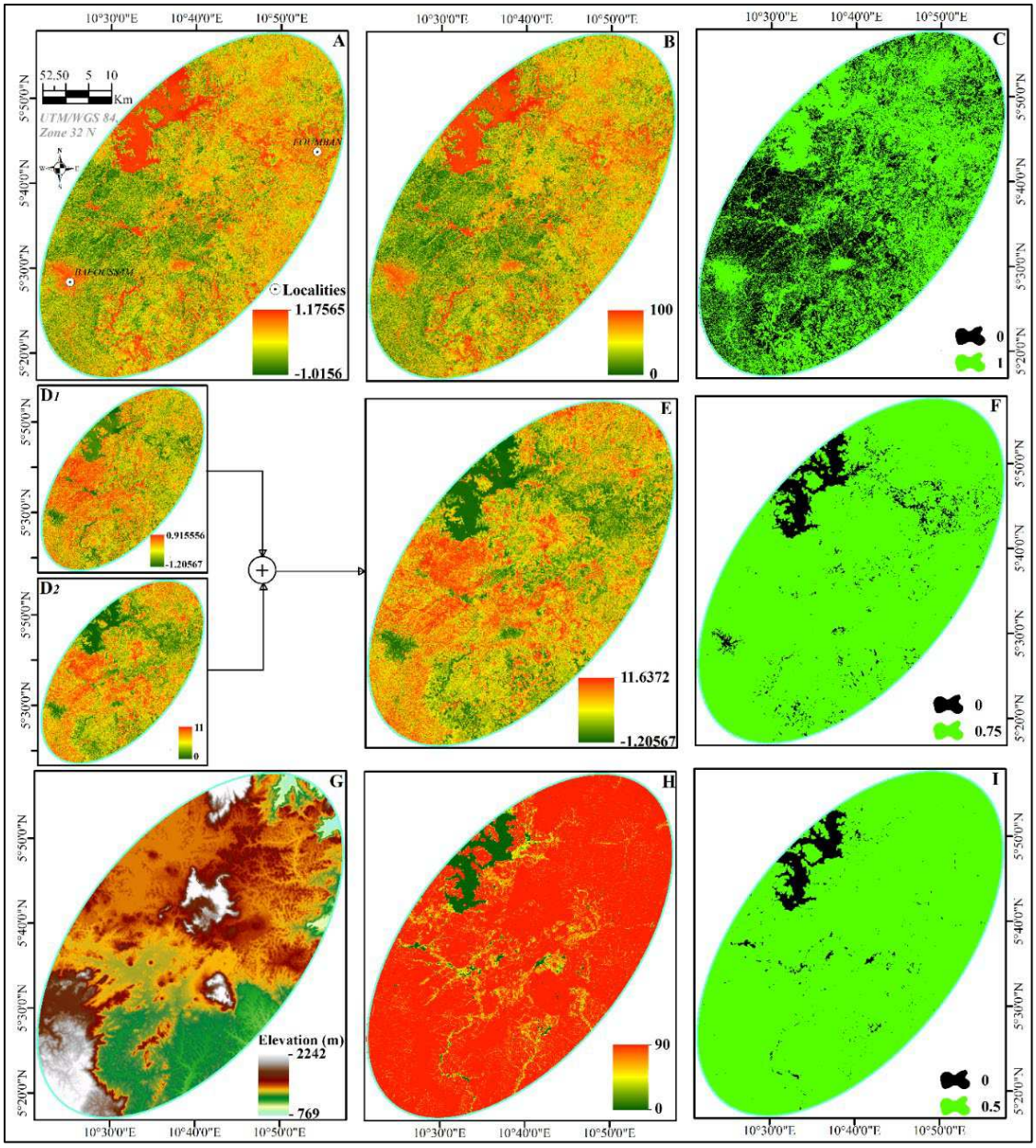

Fig.6. SLIP stretched and conditioned layers. *A) INDVI stretched values; B) Barren land binned map; C) MNMDI + hydrothermal stretched map; D) Land moisture binned map; E-Slopes in degrees; F-Slopes binned map*.

Only remains the triggering factor identified as a long and huge rainfall condition. The DRIP algorithm helps assessing it.

Adapted DRIP algorithm

The DRIP tool is adapted as the rainfall intensity and threshold corresponding to the SLIP landslide mapping. Monthly precipitations of the west Cameroon were computed between 1948 and 2017 for Africa[8], and annual data are available for 2018 and 2019[9] (Table 2). According to the Tropical Applications of Meteorology using Satellite

[8] https://fr.climate-data.org/afrique/cameroun/west-1367/
[9] https://weather-and-climate.com/average-monthly-Rainfall-Temperature-Sunshine

and ground-based observations (TAMSAT) data, especially its TRMM Multi-satellite Precipitation Analysis (TMPA) datasets component and mapping models, daily rainfall for the Cameroons' west highlands were between 6 mm and more than 10 mm between 1983 and 2012 (Maidment et al., 2014). The annual highest period is between the second decade of June and the first decade of October, with at least 15 millimeters to more than 25 millimeters per day (Maidment et al., 2014; Dezfuli et al., 2017).

Fieldwork observations and data collection assessed the rainfall of 27 to 28 October in Bafoussam up to 81 mm, in about 36 hours, before the landslide (Local agro-meteorology offices; October 2019). This represents *22.0%* of the 384 mm recorded for that monthly rainfall in 2019 (Appendix 2). Ten groups of rainfall records were determined with five months of rainfall, from June to October, i.e. 50 observations (Appendix 2). The month's selection is explained by the fact that all the landslides in Cameroon occurred in that interval, corresponding to the full rainy season (Table2.). Since the 50's, more than 136 deaths were recorded, before 2019 (Tchindjang, 2012 & 2013).

The rainfall increases then from June to September with higher records in August, and decreases in October. The trends are the same for the number of rainy days, although some local differences can be barely noticed between two zones. In addition, the rainfall zonation was done from the lower (Zone 1) to the higher (zones 9 and 10) records. Histograms of zones 1, 5 and 9 illustrate these two statements for 2019 (Fig.7).

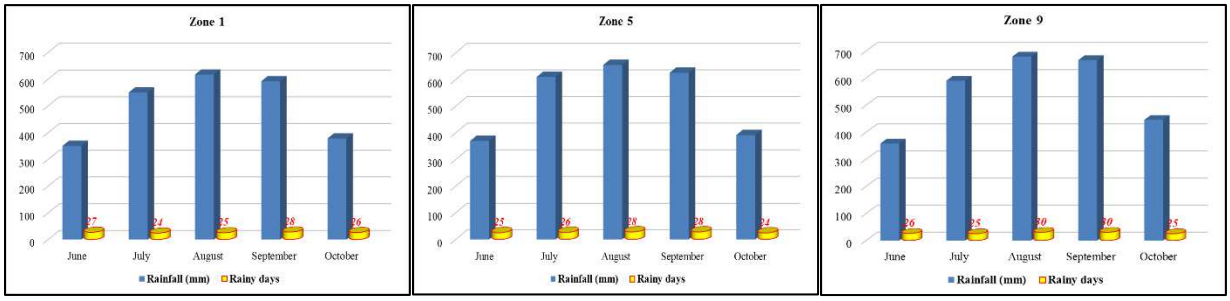

Fig.7. Monthly rainfall and rainy days sampled for three zones of the study area in 2019

The general trends give an average rainfall of 2615 mm for 1948-2018 and 2573 mm in 2019, representing respectively *79%* and *78%* of the 3300 mm maximum annual rainfall. The month of August usually represent *25%* of the five months, while October when occurred the recent landslide record about *14%* (Fig.8). Moreover, the 80 mm preceding the landslide represents *3.1%* of the five months rainfall and almost four times the total daily mapped by Maidment et al. (2014) and Dezfuli et al. (2017).

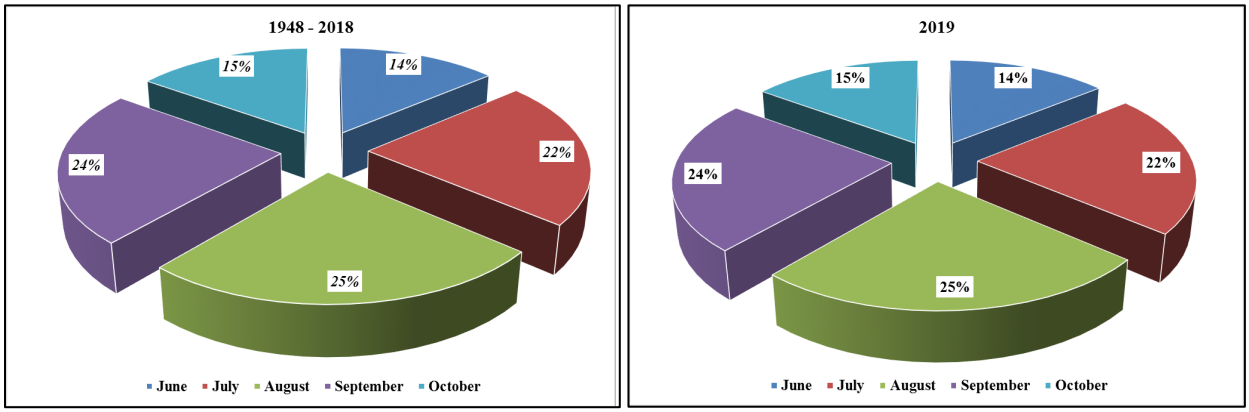

Fig.8. Percentages of monthly rainfall For June-October period

Table 2. Landslides history and consequences in Cameroon to the best of the records

	Location (Region)	*Month / Year*	*Main casualties and losses*
1	Fossong-Wentcheng (Dschang)	August / 1978	6 Deaths reported and plantations destroyed
2	Pinyin (North-West)	June / 1991	Plantations destroyed
3	Santa (Bamenda)	September 12 / 1992	12 deaths reported
4	Bafaka (North-west)	1993	Plantations and houses destroyed
5	Rom Nwah	2000	6 deaths reported, plantations destroyed
6	Limbe (South-west)	2001 & 2009	24 deaths reported, 2800 homeless
7	Bana (West)	September 10 / 2002	10 deaths reported
8	Maga (Far-North)	July 20/2003	22 deaths reported, 50 deaths cattle
9	Bafou (West)	2003	2 deaths reported
10	Wabane (South-west)	2003	1 death reported
11	Fondonera (West)	2008	Plantations destroyed
12	Abuh (North-West)	September 27 / 2007	Plantations destroyed
13	Moume-Bafang (West)	2008	1 death reported, 100 homeless, national road destroyed/cut and 9 months without traffic
14	Bamenda (North-West)	2009	7 deaths, 50 homeless, road destroyed
15	Koutaba (West)	October 23 / 2011	2 deaths reported
16	Mbo and Ndop plain (West and North-West)	August, September and October every year	Plantations and road destroyed
17	Foumban (West)	September 4-5 / 2018	Houses destroyed and access roads destroyed
18	Bafoussam (West)	October 28-29/2019	45 deaths reported, 300 homeless and dozens of houses destroyed

After the data collection, their statistical distribution and variability were assessed. One popular method is the Weibull distribution that is expressed by calculating a cumulative distribution (CDF) or a probability density function (PDF) using the following equation:

$$\mathbf{f(x)} = \frac{\gamma}{\alpha}\left(\frac{\mathbf{x-\mu}}{\alpha}\right)^{\boldsymbol{\gamma-1}} \mathbf{exp}(-((\mathbf{x}-\boldsymbol{\mu})/\boldsymbol{\alpha})^{\boldsymbol{\gamma}}) \qquad \text{With} \quad \mathbf{x} \geq \boldsymbol{\mu}; \boldsymbol{\gamma}, \boldsymbol{\alpha} > \mathbf{0}$$

Where γ is the shape parameter, μ is the location parameter and α is the scale parameter. Because the Weibull model assesses strength and failure of a system in relation with time (Klein, 2009), the resistant parts or particles expressed the strength to failure and lifetime probability of the system. If $\boldsymbol{\gamma < 1}$, then the failure rate decreases with time; if $\boldsymbol{\gamma = 1}$, the rate of failure remains constant with random weaknesses; if $\boldsymbol{\gamma > 1}$, the rate of failure increases with time, also expressed as ageing process. In this case, we assess the stronger relationship to the failures in the relationship between rainfall and days of rainfall for the period 1948-2018 average, setting $\boldsymbol{\gamma = 0.5}$.

The rainfall data were scaled on a daily window by the ratio [*monthly rainfall over monthly total of rainy days*]. Further, the ratio of [*monthly rainy days over monthly total days*] was computed. The probabilities of failure and success were defined for both sets of data as:

$$\mathbf{PF(x)} = \frac{\mathbf{n_x}}{\mathbf{N+1}}$$

$$\mathbf{PS(x)} = \mathbf{1 - PF}$$

With *PF* and *PS* representing the probability of strength to failure and the probability of success. Then, their probabilities of strength to failure are suitable to be used as the *z* value in the standard PDF computation, which is defined as a normal distribution. Purposely and based on the data, the averages (≈*3* and ≈*4*) and the standard deviations (≈*1*) of the daily rainfall and days of rainfall were computed for the two periods, and the PDF curves were superimposed on each other to find intersections(Fig.9a&b).

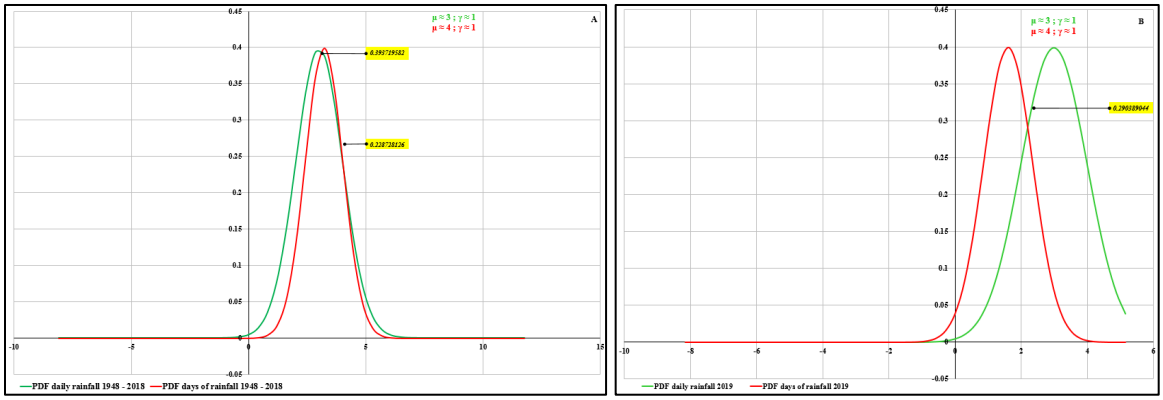

Fig.9. Individual PDF curves and their intersections before (A) and in (B) 2019

From the intersections of the two PDF curves, a set of thresholds were defined in a whole algorithm, with six explanatory variables (X), and two response variables (Y). The algorithm is written as follow:

i. $X_{1.1.} = \begin{cases} \mathbf{1} & if\ PDF\ daily\ rainfall\ frequency\ \leq 0.228728126 \\ \mathbf{0} & Otherwise \end{cases}$

ii. $X_{1.2.} = \begin{cases} \mathbf{1} & if\ 0.228728126 > PDF\ daily\ rainfall\ frequency\ \leq 0.393719582 \\ \mathbf{0} & Otherwise \end{cases}$

iii. $X_{1.3.} = \begin{cases} \mathbf{1} & if\ 0.393719582 > PDF\ daily\ rainfall\ frequency \\ \mathbf{0} & Otherwise \end{cases}$

iv. $X_{2.1.} = \begin{cases} \mathbf{1} & if\ PDF\ days\ of\ rainfall\ frequency\ \leq 0.228728126 \\ \mathbf{0} & Otherwise \end{cases}$

v. $X_{2.2.} = \begin{cases} \mathbf{1} & if\ 0.228728126 > PDF\ days\ of\ rainfall\ frequency\ \leq 0.393719582 \\ \mathbf{0} & Otherwise \end{cases}$

vi. $X_{2.3.} = \begin{cases} \mathbf{1} & if\ 0.393719582 > PDF\ days\ of\ rainfall\ frequency \\ \mathbf{0} & Otherwise \end{cases}$

vii. $Y_1 = \begin{cases} \mathbf{1} & if\ PDF \leq 0.290389044 \\ \mathbf{0} & Otherwise \end{cases}$

viii. $Y_2 = \begin{cases} \mathbf{1} & if\ 0.290389044 > PDF \\ \mathbf{0} & Otherwise \end{cases}$

As Y_2 expresses the opposite perfect of Y_1, it has been decided to use one or another as response variable instead of both. Then the probability of rainfall-triggered landslide is calculated by performing the logistic function.

In fact, logistic regression is a classification algorithm useful for predicting binary outcome (1/0, Yes/No, True/False) given a set of predictor variables. It allows computing a multivariate regression relation between a binary dependent variable and several independent variables (Atkinson and Massari, 1998). Multiple logistic regression assumes that the observations are independent and the natural log of the odds ratio and the measurement variables have a linear relationship. The quantitative relationship between the occurrence and its dependency on several variables can be expressed as:

$$P_{(Ev=1)} = \frac{1}{1 + e^{Z_{Ev.}}}$$

Where P_{Ev}, is the probability of an event occurring. In this case, the event is the daily rainfall threshold to trigger the landslide, and then being equal to *1* in the interval (*0*; *1*). $Z_{Ev.}$ is the linear relationship of the event occurrence's with the independent variables and it is expressed as:

$$\mathbf{Z_{Ev} = b_0 + b_1 x_1 + b_2 x_2 + \cdots b_n x_n}$$

Where b_0 is the intercept of the model, the $\boldsymbol{b_i}$ (i=0, 1, 2, … , n) are the slope coefficients of the logistic regression model, and the $\boldsymbol{x_i}$ (i=0, 1, 2, … , n) are the explanatory variables. Fig.10 present the main steps of the DRIP modelling.

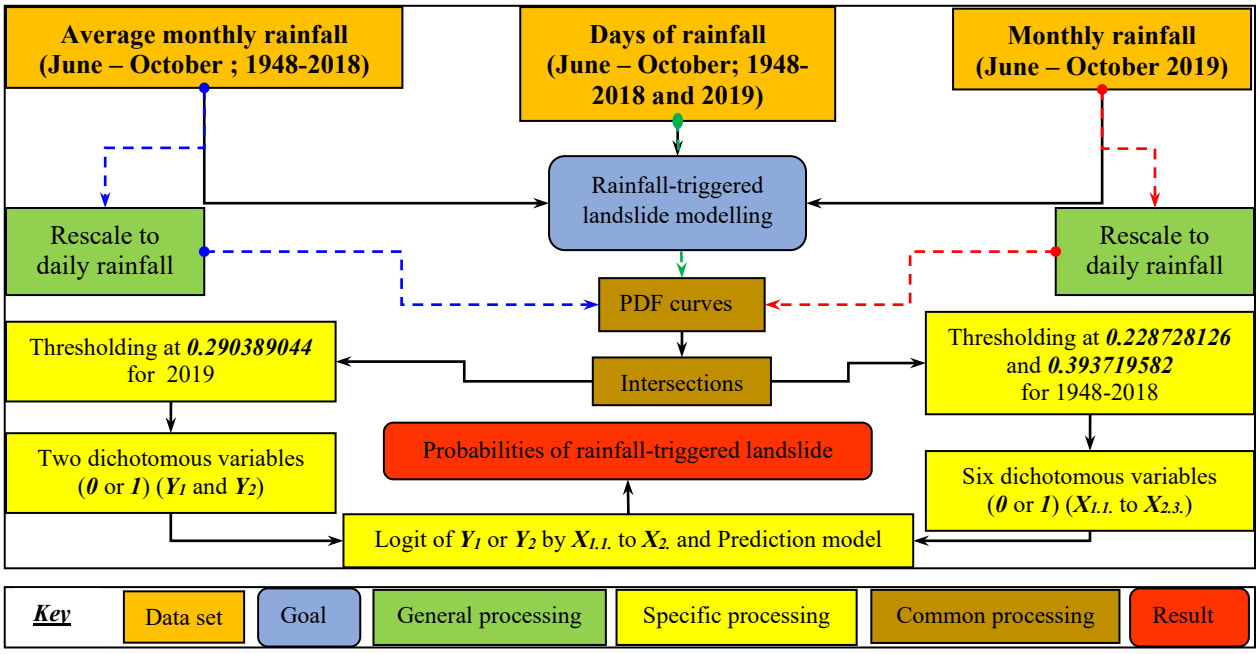

Fig.10. Workflow of the DRIP process

The graphical representation of the logit models, known as receiver operating characteristic (ROC) curve, was used to assess the quality of the prediction. It represents a plot of the sensitivity, i.e. the *TP* rate (*TPR*), against one minus the specificity, i.e. the *FP* rate (*FPR*), as the values of the cut-point *c* increase from *0* through *1*. The *TPR* is the ratio of all positive cases correctly predicted under a specific threshold value. *FPR* is the ratio of all negative cases that are incorrectly predicted to be positive, under the same threshold value. They are expressed by the following equations:

$$\mathbf{TPR = TP/(TP + FN)}$$

$$\mathbf{FPR = FP/(FP + TN)}$$

When the ROC curve matches the top-left corner of the plot, it explains then the excellent quality of the model. The implication on the *TPR-FPR* analysis concerned the area under the ROC curve (AUC), which helps summarizing the discrimination ability of a model. It ranges between *0.5* or no discrimination ability and *1* or perfect discrimination.

Results and findings

The LHZ map in relation to recent landslides events

The SLIP outcome is a map identifying the landslides zones of occurrences and predictions in eight classes. Its values vary from *0* to *2.25*, based on the bin values affected to each layer. The lowest value, *0*, stands for unmet conditions and the highest value, *2.25*, corresponds to the landslides areas (Table 3).

Table 3. LHZ codes and explanation

Classes codes	Conditions met
0	None
0.5	Slopes
0.75	Soil moisture
1	Uncovered soil
1.25	Soil moisture & Slopes
1.5	Uncovered soil & Slopes
1.75	Uncovered soil & Soil moisture
2.25	Uncovered soil & Soil moisture & Slopes

Visually, the entire subset is widely exposed to landslides hazard (Fig.11.). Non-vegetated mountain flanks are the most exposed and because all the area's slopes far above 75º, the conditions are fulfilled for a landslide according to the algorithm developed (Fig.11.). The accuracy of the method and the validation is performed by zooming on the two localities of Foumban and Bafoussam, subject to landslides of September 2018 and October 2019. Indeed, when plotted on the LHZ's map as recorded on the closest point on the field, the landslides sites of Njiloum (1&2) and Njitout, in Foumban, as well as Gouache in Bafoussam match the red zone with code *2.25*, i.e. a *100%* mapping. Moreover, three on five (3/5) sites of observations around the Gouache landslide events coordinates belongs to the red zone, while the two others are intermediate between this exposure zone and the class coded *1.75* (Fig.11.). Then, 7/9 points belong to the landslide occurrence class, i.e. *77.8%* of overall accuracy. Further, these two cities meet at least two conditions for the landslide occurrence, mainly the soil exposure and the soil moisture that have the second ranked class when combined, i.e. *1.75* (Fig.11.).

Therefore, the LHZ map based on the SLIP algorithm shows that landslides affected area, i.e. where the three conditions are fully fulfilled (*2.25*), is 224 110 hectares, representing about *57.02%* of the studied area (Fig.12). The second high area is occupied by class *1.25* (soil moisture and slopes), with 139549 hectares, i.e. *35.5%* of the study area. Then, classes *1.75* (uncovered soil and soil moisture) and *1.5* (uncovered soil and slopes) concern reduced areas (*0.56%* and *3.18%*), while the lowest value, *0*, just concern 2 hectares (*0.00056%*).

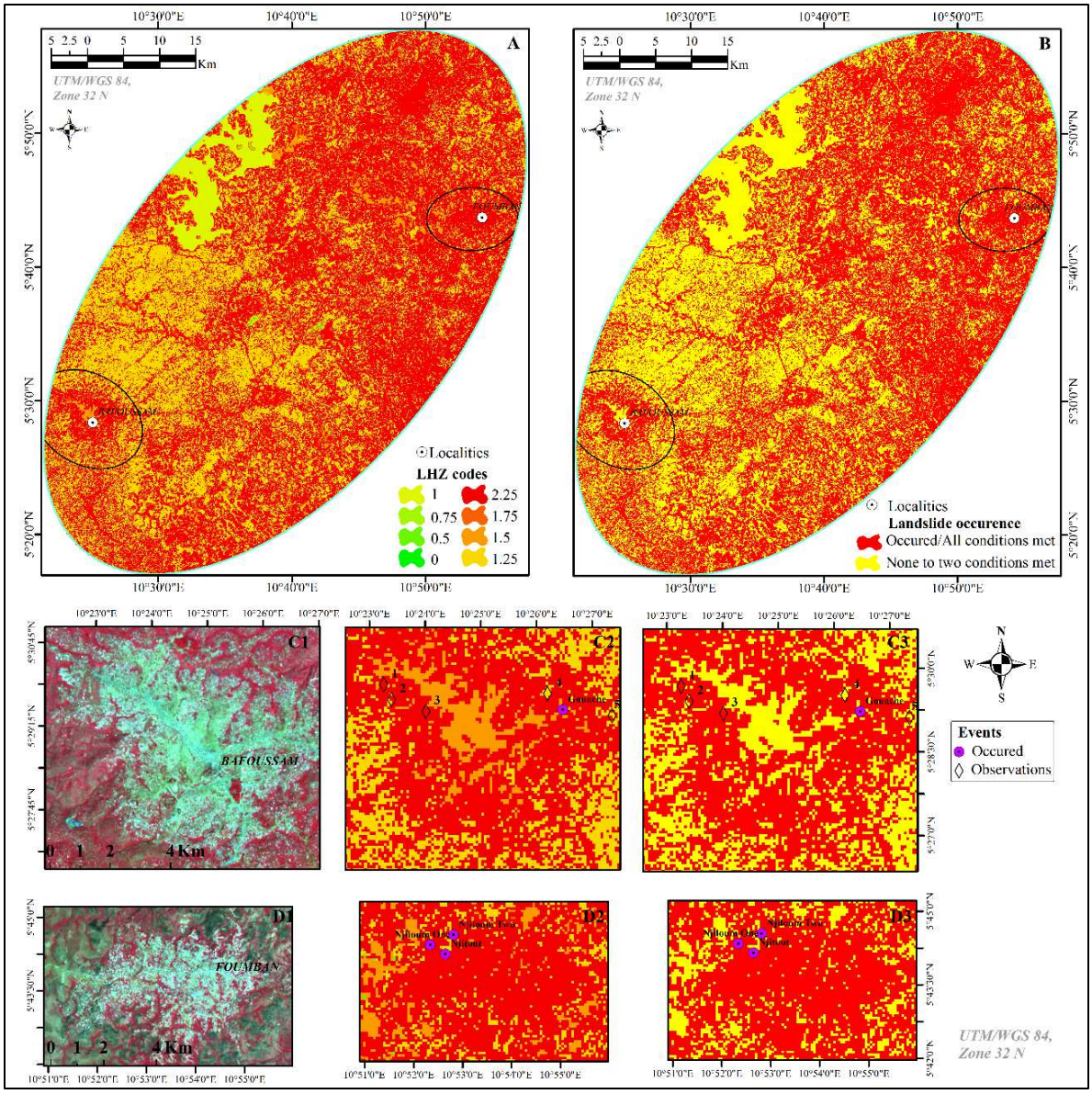

Fig.11. LHZ mapping. *A) The eight classes and codes. B) Class 2.25 versus the other classes. C1) to C3) Patterns and accuracy assessment in Bafoussam. D1) to D3) Patterns and accuracy assessment in Foumban*

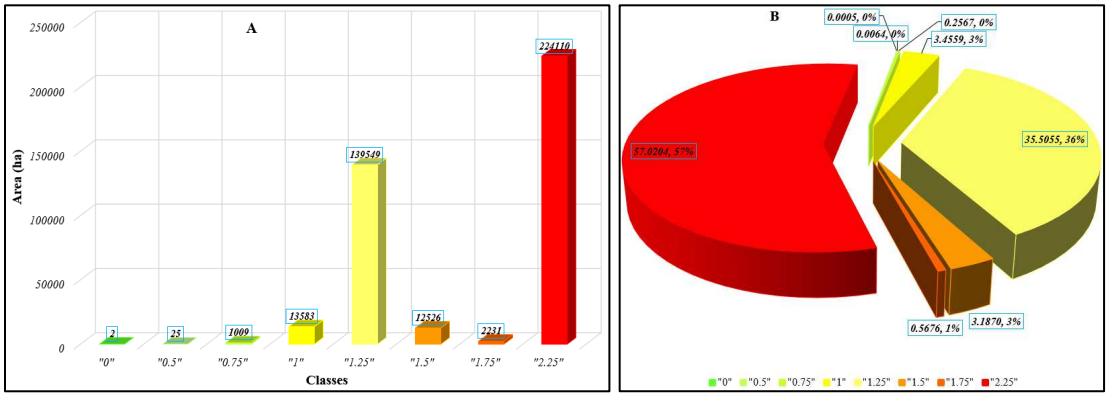

Fig.12. Areas (A) and percentages (B) of LHZ per classes

Rainfall as landslides triggering factor

A comment on statistics of daily rainfall and days of rainfall reveals major information related to landslides occurrences and confirming existing records. Taking the daily rainfall average in period 1948-2018 and interval June-October, the lowest values were in recorded in June, between 13.6 mm/day and 16.13 mm/day, while the highest values were recorded in August between 22.3 mm/day and 25.9 mm/day. These illustrations confirm at first sight the TRMM Multi-satellite Precipitation Analysis (TMPA) for the study area between 15 mm/day and 25 mm/day inside de same monthly interval (Maidment et al., 2014; Dezfuli et al., 2017). In addition, the ratio of days of rainfall appraisal gives the lowest value to October with *0.618* (*61.8%*), while the highest value is the maximum *1* (*100%*), for August.

Further, a visual appraisal of maps outputted from these data shows a decreasing spatial distribution from the south to the north, and highlights three main spots (Fig.13). The largest and densified spot is in the southern area, the second one is in the west and the third one is in the northeast area (Fig.13). The first and the third spots concern the areas inside and around the localities of Bafoussam and Foumban where landslides of 2018 and 2019 occurred. At first glance and according to a visual comparison with the SLIP algorithm outputs, it may be assumed that rainfall can trigger the landslides in these areas. However, the statistical analysis of the logit model helps to comfort and discuss this assumption.

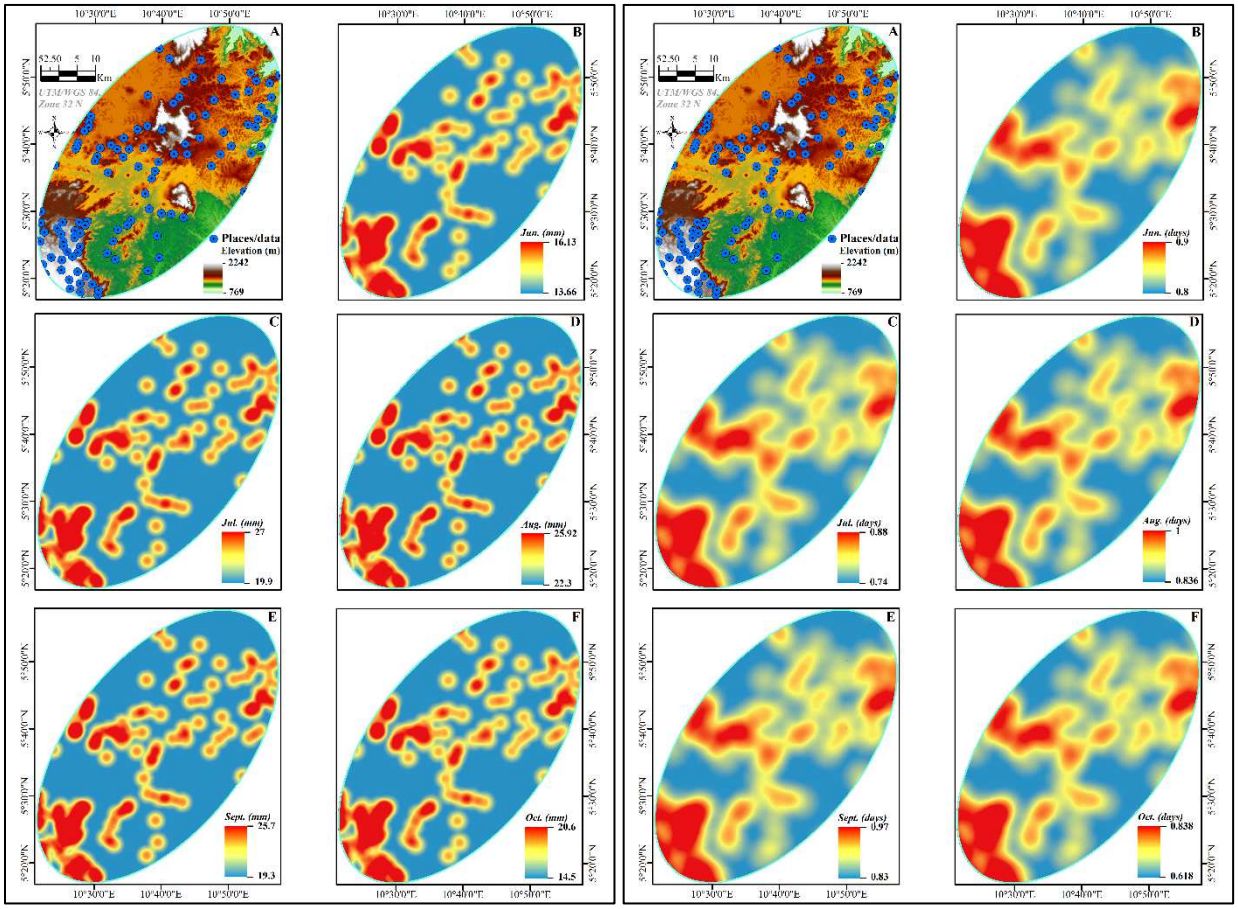

Fig.13. Daily rainfall (left) and days of rainfall (right) spatial distribution

According to the logit model, the prediction of landslides-triggered threshold is expressed as follow:

$$\mathbf{Pred(Y.1.)} = \mathbf{1} / (\mathbf{1} + \mathbf{exp}(-(-\mathbf{17.3384002171496} + \mathbf{20.3088146827193} * \mathbf{X.1.1} - \mathbf{1.27218133241455E-09} * \mathbf{X.1.2.} + \mathbf{3.47429895467361E-10} * \mathbf{X.1.3.} + \mathbf{1.55185644192548E-10} * \mathbf{X.2.2.} - \mathbf{1.57206861984972E-09} * \mathbf{X.2.3.})))$$

At first point, it appear that the standardized coefficient of each explanatory variable is low and around zero. The three highest coefficients are those of $X_{1.1.}$, $X_{1.2.}$ and $X_{2.3.}$ (Fig.14.)

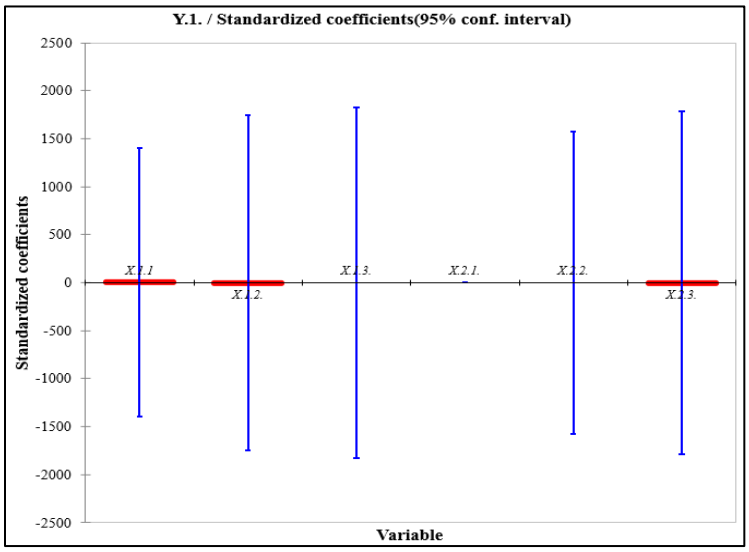

Fig.14. The standardized coefficients of the explanatory variables

To better assess the contribution of each explanatory variable coefficient on the model, the functions of all the thresholds were extracted from the general prediction model. Therefore, the probability for landslides-triggered is divided onto nine functions (Table 4.).

Table 4. Different probabilities expressed by the prediction model

Probability / For	$f_{(Y_1)} \leq 0.290389044$	
	Expression	***Outcome***
$f_{(X_1)} \leq 0.228728126$ **and** $f_{(X_2)} \leq 0.228728126$	$1 / 1 + \exp(-(-17.3384002171496 + 20.3088146827193))$	***95.122%*** *risk for landslides*
$f_{(X_1)} > 0.228728126$ *and* ≤ 0.393719582 **and** $f_{(X_2)} > 0.228728126$ *and* ≤ 0.393719582	$1 / 1 + \exp(-(-17.3384002171496 - 1.27218133241455E-09 + 1.55185644192548E-10))$	***99.99%*** *chance of no-landslides*
$f_{(X_1)} > 0.393719582$ **and** $f_{(X_2)} > 0.393719582$	$1 / 1 + \exp(-(-17.3384002171496 + 3.47429895467361E-10 - 1.57206861984972E-09))$	***99.99%*** *chance of no-landslides*
$f_{(X_1)} \leq 0.228728126$ **and** $f_{(X_2)} > 0.228728126$ *and* ≤ 0.393719582	$1 / 1 + \exp(-(-17.3384002171496 + 20.3088146827193 + 1.55185644192548E-10))$	***99.58%*** *chance of no-landslides*

$f_{(x_1)} \leq 0.228728126$ **and** $f_{(x_2)} > 0.393719582$	$1 / 1 + \exp(-(-17.3384002171496 + 20.3088146827193 - 1.57206861984972E-09))$	***98.85%** chance of no-landslides*
$f_{(x_2)} \leq 0.228728126$ **and** $f_{(x_1)} > 0.228728126$ *and* ≤ 0.393719582	$1 / 1 + \exp(-(-17.3384002171496 + 3.47429895467361E-10))$	***99.99%** chance of no-landslides*
$f_{(x_2)} \leq 0.228728126$ **and** $f_{(x_1)} > 0.393719582$	$1 / 1 + \exp(-(-17.3384002171496 + 1.55185644192548E-10))$	***99.99%** chance of no-landslides*
$f_{(x_1)} > 0.228728126$ *and* ≤ 0.393719582 **and** $f_{(x_2)} > 0.393719582$	$1 / 1 + \exp(-(-17.3384002171496 - 1.27218133241455E-09 + -1.57206861984972E-09))$	***99.99%** chance of no-landslides*
$f_{(x_2)} > 0.228728126$ *and* ≤ 0.393719582 **and** $f_{(x_1)} > 0.393719582$	$1 / 1 + \exp(-(-17.3384002171496 + 1.55185644192548E-10 + 3.47429895467361E-10))$	***99.99%** chance of no-landslides*

From the table 4 above, two main cases are to be noticed, as rainfall-triggered landslides event, Y_1 to happen or not. On one hand, there is *95.122%* risk for landslides, when crossing frequency of daily rainfall and days of rainfall is under or at *29.04%* and both of their individual frequencies are under or at *22.87%*, (green row in table 4). On the other hand, the remaining eight probabilities refer to the 'no-landslide' event ($\mathbf{1 - Y_1}$), when considering all the others individual threshold of daily rainfall and days of rainfall (Orange row in table 4). The lower value is *98.85%* chance of not having landslides, when daily rainfall frequency is under *22.87%*, and days of rainfall frequency is over *39.37%*, for the same crossing threshold under or at *29.04%*. All the others probabilities of 'no-landslide' are up to *99.99%*. Therefore, the adapted DRIP approach shows suitability to distinguish landslide and no-landslide for one common frequency. Its prediction model can be trusted according to an accuracy assessment. From the classification table, the true positive rate (TPR) or sensitivity is *100%* (39/39), while the false positive rate (FPR) or specificity is *82%* (Table 5.)

Table 5. Classification table for the training sample – variable Y_1.

To / **From**	0	1	*Total*	*%Correct*
0	9	2	11	***81.82***
1	0	39	39	***100***
Total	***9***	***41***	***50***	***96***

The ROC curve assessing the trade-off between the TPR and FPR was plotted at a cut-point *c* settled at ***0.5***. The curve is close to the upper-left corner of the graph, testifying the good quality of the prediction (Fig.15.). For a complete model performance interpretation, the area under the ROC curve (AUC) values can be classified in five levels (Xiong et al., 2020): 0.5~0.6 = poor, 0.6~0.7 = moderate, 0.7~0.8 = acceptable, 0.8~0.9 = excellent and 0.9~1 = almost perfect. Therefore, with an AUC of ≈*0.82* (Fig.15.), the prediction model is rated as excellent.

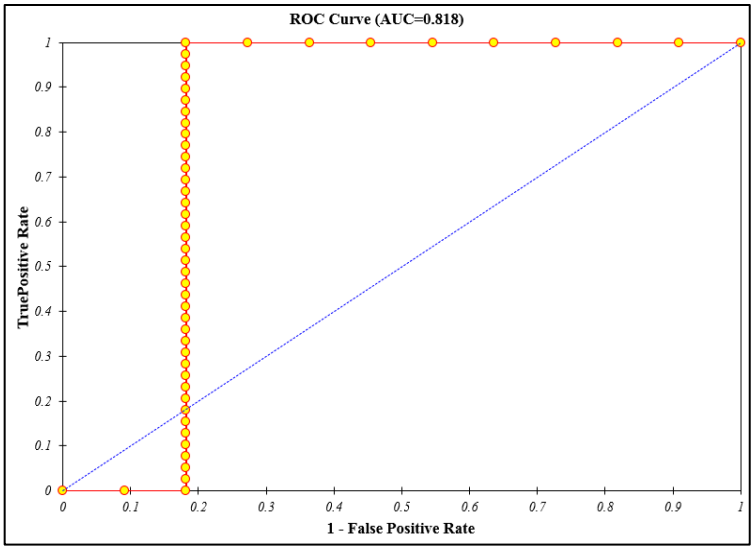

Fig.15. The Receiver Operating Curve of the model

Caveats and outlooks

The two algorithms of SLIP and DRIP as originally developed (Fayne et al., 2018), and adapted in this research connect landslides occurrence and huge rainfall. Here, as the hourly rainfall data are not available and knowing that the original DRIP algorithm correlate the two events in a hourly window, this model used as is in other areas should be considered only for a daily scale. The ongoing work also concerns the automatic mapping and crossing of DRIP and with the SLIP outcomes as continuous as possible. The goal is to predict and correlate daily rainfall, days of rainfall and the magnitude of the landslide in terms of speed of occurrence, to complete the status mapping and timely retrospective of the original algorithms. Moreover, it will be interesting to correlate the soil stability/instability with the daily/hourly rainfall. This will help sequencing the soil moisture and stability/instability chronology on the scale chosen, and verify if the highest positive correlation matches landslide occurrence.

In addition and far beyond the above mentionned aspects, the built-up extent and material can introduce biases especially when computing soil spectral indices (Ngandam et al, 2019). For instance, cities as Bafoussam and Foumban are characterized by their mi-rural/mid-urban patterns that include many houses in raw material such as earthen bricks and straw roofs, or unpaved dusty/muddy roads and tracks. Therefore, their reflectance with the landslide-affected areas might cause biases in the INDVI computation because they usually reflect enough in the red and SWIR wavelengths of Landsat 8 images (Ngandam et al, 2019). Then, the ongoing improvements also consider built-up spatial evolution and cities metabolism for further experimentations.

Conclusions

This paper has aspired to adapt the SLIP and the DRIP algorithms to map and predict the rainfall-triggered landslide in west-Cameroons' highlands. The first axe has been to produce a LHZ map, mainly locating the recent event of the 28 October 2019 in Bafoussam, and in parallel the event of 4 and 5 September 2018 in Foumban. Using three layers that are the soil exposure, the soil moisture and the slope degrees, a SWLC has helped combining them to produce a map zonation accurate at *100%* for the landslides occurred and *77.8%* for the control points. Further, using the logit regression, probability of the rainfall-triggered landslide is up to *95%*, and the no-landslide is up to *99.99%*, under or

at the daily rainfall and the days of rainfall common frequency of *29.04%*. This prediction model is trustable at *82%* according to the AUC. Therefore, although improvements and comparisons with others models are in perspective, the proposed methodology contributes to another vision of the SLIP and DRIP algorithms, offering a new alternative in case of voids and gaps between data.

Acknowledgements

In memory of the 45 deaths and dozens of other victims (injured, homeless) reported for the 28 October 2019 landslide in Bafoussam. In support of Cameroons' government, NGOs and civil groups actions against geohazards.

Authors' contributions

The first two authors conceived, carried out the research and mapping, drafted the manuscript and finalized the corrections. The first and the third authors directed and validated the statistical process and modelling. The whole team contributed to fieldwork, data collection and curation, method validation, literature sourcing, mapping, editing, structuring and critical reviewing. All authors read and approved the final manuscript.

Funding

The private consulting firm StatsN'Maps, through its *'Research Support Funds'* (SN'M-RSF), financially supported the purchase of articles and books chapters not free, as well as all the fieldwork investigations concerning rainfall data acquisition. The licenses of Erdas 2020 version 16.6.0.1366, ArcGisPro version 2.5 and XLStats 2020.1.64570 software used in this research are properties of StatsN'Maps and available upon request.

Availability of data and materials

All the data and material used for this research were incorporated as needed to the text or added as appendixes. For all other details needed, contact us via *stats.n.maps.expertise@gmail.com*

Competing interests

The authors declare that they have no competing interests.

References

Ayonghe SN, Suh CE, Ntasin EB, Samalang P & Fantong W, (2002) Hydrologcally, seismically and tectonically triggered landslides along the Cameroon Volcanic Line, Cameroon. Africa Geosciences Review, 9:4, 325-335.

Blahut, J, VanWesten, C, Sterlacchini, S (2010) Analysis of landslide inventories for accurate prediction of debris-flow source areas. Geophys J Roy Astron Soc., 119:36–51.

Brabb, E (1993) Proposal for worldwide landslide hazard maps. In: Novosad, S & Wagner, P (eds.) Proceedings of the 7th International Conference and Workshop on Landslides. Balkema, AACzech and Slovak Republics, 15-27.

Braun, SA (2011) "TRMM Status," 7th GPM International Planning Workshop, Tokyo, Japan, Dec. 5-7. URL: http://www.eorc.jaxa.jp/GPM/ws7/pdf/5thDEC2007/AM/5_am06.pdf

Brusden, D (1984) Mudslides. In: Brusden, D, Prior, D, editors. Slope Instability. Chichester: Wiley, pp. 363–418.

Bui, D, Pradhan, B, Lofman, O, Dick, O (2012) Landslide susceptibility assessment in the Hoa Binh Province of Vietnam: a comparison of the Levenberg-Marquardt and Bayesian regularized neural networks. Geophys J Roy Astron. Soc., 171–172:12–29.

Calvello M, Cascini L, Mastroianni S (2013) Landslide zoning over large areas from a sample inventory by means of scale-dependant terrain units. Geophys J Roy Astron Soc., 182:33–48.

Colombo, A, Lanteri, L., Ramasco, M. and Troisi, C. (2005) Systematic GIS-based landslide inventory as the first step for effective landslide-hazard management. Landslides 2:4, 291-301.

Couture, R (2011) Landslide Terminology - National Technical Guidelines and Best Practices on Landslides. Geological Survey of Canada, Open File 6824, 12 p.

Crozier, MJ (1986): Landslides: Causes, Consequences and Environment. London and Sidney, Croom Helm Limited, 252 p.

Cruden, DM (1991) A simple definition of landslide. Bulletin of international association of Engineering Geology, 43:1, 27-29.

Dezfuli, AK, Ichoku, CM, Mohr, KI and Huffman, GJ (2017) Precipitation characteristics in West and East Africa from satellite and in situ observations. Journal of Hydrometeorology, 18:6, 1799-1805.

Elsheikh, AA, Gao, SS, Liu, KH (2014) Formation of the Cameroon Volcanic Line by lithospheric basal erosion: Insight from mantle seismic anisotropy. Journal of African Earth Sciences, 100: 96–108.

Fayne, JV, Ahamed, A, Roberts-Pierel, J, Rumsey, AC, Kirschbaum, DB (2019) Automated Satellite-Based Landslide Identification Product for Nepal. Earth Interactions, 23:3, 23p.

Galli, M, Ardizzone, F, Cardinali, M, Guzzetti, F, Reichenbach, P (2008) Comparing landslide inventory maps. Geomorphology, 94:268–289.

Garosi, Y, Sheklabadi, M, Pourghasemi, HR, Besalatpour, AA, Conoscenti, C., Oost, KV (2018) Comparison of differences in resolution and sources of controlling factors for gully erosion susceptibility mapping. Geoderma 330: 65–78.

Gosh, K, Bandyopadhyay, S, Kumar De, S (2011) A Comparative Evaluation of Weight-Rating and Analytical Hierarchical (AHP) for Landslide Susceptibility Mapping in Dhalai District, Tripura. Environment and Earth Journal Observation, pp. 175-193.

Guzzetti, F, Reichenbach, P, Cardinali, M, Galli, M and Ardizzone, F (2005) Probabilistic landslide hazard assessment at the basin scale. Geomorphology 72: 272– 299.

Guzzetti, F, Carrara, A, Cardinali, M, Reichenbach, P (1999) Landslide hazard evaluation: a review of current techniques and their application in a multi-scale study, Central Italy. Geomorphology, 31:181-216.

Hutchinson, JN (1988) General Report: Morphological and geotechnical parameters of landslides in relation to geology and hydrogeology. Proceedings, Fifth International Symposium on Landslide*s*, Rotterdam: Balkema, (Ed: Bonnard, C.), 1:3-35.

Jiménez-Perálvarez, JD, Irigaray, C, El Hamdouni, R, and Chacón, J (2011) Landslide-susceptibility mapping in a semi-arid mountain environment: An example from the southern slopes of Sierra Nevada (Granada, Spain). Bull. Eng. Geol. Environ., 70:265–277.

Kankeu B & Ntchantcho R (2019) Natural disasters in Gouache-Bafoussam, scientific causes. Translated from French original version. Mission report, Institute of Geological and Mining Research's Directorate General. Report, 14 p.

Kanungo, DP, Arora, MK, Sarkar, S, Gupta, RP (2006) A comparative study of conventional, ANN black box, fuzzy and combined neural and fuzzy weighting procedures for landslide susceptibility zonation in Darjeeling Himalayas. Eng. Geol, 85:3–4, 347–366.

Kanungo, D, Arrora, M, Sarkar, S, Gupta, R (2009) Landslide Susceptibility Zonation (LSZ) mapping-a review. J South Asia Disaster Stud, 2:81–105.

Kayastha P, Dhital M. De Smedt F (2013) Application of the analytical hierarchy process (AHP) for landslide susceptibility mapping: a case study from the Tinau watershed, west Nepal. Comput Geosci 52:398–408.

Kirschbaum, DB, Adler, R, Hong, Y, Lerner-Lam, Al (2009) Evaluation of a satellite-based landslide algorithm using global landslide inventories. Nat. Hazards Earth System Sci, 9:673-686.

Klein, CA (2009) Characteristic strength, Weibull modulus, and failure probability of fused silica glass. Optical Engineering, 48, 113401.

Komac, M (2006) A landslide susceptibility model using the Analytical Hierarchy Process method and multivariate statistics in perialpine Slovenia. Geomorphology 74:1, 17-28.

Lee, S (2005) Application of logistic regression model and its validation for landslide susceptibility mapping using GIS and remote sensing data. Int. J. Remote Sens., 7:1477–1491.

Lee, C, Huang, C, Lee, J, Pan, K, Lin, M, Dong, J (2008) Statistical approach to storm event-induced landslides susceptibility. Nat Hazards Earth Syst Sci., 8:941–960.

Lin, L, Lin, Q, and Wang, Y (2017) Landslide susceptibility mapping on a global scale using the method of logistic regression. Nat. Hazards Earth Syst. Sci., 17, 1411–1424. https://doi.org/10.5194/nhess-17-1411.

Maidment, RI, Grimes, D, Allan, RP, Tarnavsky, E, Stringer, M, Hewison, T, Roebeling, R and Black, E (2014) The 30 year TAMSAT African rainfall climatology and time series (TARCAT) dataset. Journal of Geophysical Research: Atmospheres, 119:18, 10619-10644.

Martha T, vanWesten C, Kerle N, Jetten V, Vinod Kumar K (2013) Landslide hazard and risk assessment using semi-automatically created landslide inventories. Geophys J. Roy Astron Soc. 184:139–150.

Meena, SR, Ghorbanzadeh, O, Blaschke, T(2019) A Comparative Study of Statistics-Based Landslide Susceptibility Models: A Case Study of the Region Affected by the Gorkha Earthquake in Nepal. Int. J. Geo-Inf. 8, 94

Ngandam Mfondoum, AH, Gbetkom, PG, Wokwenmendam Nguet, P, Cooper, R, Hakdaoui, S (2019) Assessing the spatial metabolism of a mid-urban/mid-rural city: the relationship built-up, vegetation, bare soil and urban heat in Foumban (west-Cameroon, Central Africa) - periods 1987 - 2003 - 2019. Third International Land Use Symposium, ILUS, 2019 - "Land use changes: trends and projections", Paris, 4-6 October, Poster.
URL: 10.13140/RG.2.2.13421.33766

Pardeshi, SD, Autade, SE, and Pardeshi, SD (2013) Landslide hazard assessment: recent trends and techniques. Springer Plus, 2013, 2:523.

Penaye, J, Ateba, B, Wokwenmendam Nguet, P, Moudioh, C (2018) Disaster of September 2018 in the Njintout and Njiloum districts of Foumban. Scientific opinion. Translated from French original version. Institute of Geological and Mining Research. Report, 15p.

Petley, D (2012) Global patterns of loss of life from landslides. Geology, 40:927–930.

Pradhan, B, Lee, S (2009) Landslide risk analysis using artificial neural network model focusing on different training sites. Int J Phys Sci., 4:001–015.

Preuth, T, Glade, T, Demoulin, A (2010) Stability analysis of human-influenced landslides in eastern Belgium. Geomorphology 120:38–47.

Sarkar, S, Kanungo, D, Patra, A, Kumar, P (2006) Disaster mitigation of debris flows, slope failures and landslides. GIS based landslide susceptibility mapping- a case study in Indian Himalaya. Tokyo, Japan: Universal Academy Press, pp. 617–624.

Singh, C, Behra, K, Rocky, W (2011) Landslide susceptibility along NH-39 between Karong and Mao, Senapati District, Manipur. J Geological Soc India, 78:559–570.

Tchindjang, M, (2012) Paradoxes and risks in Cameroons' highlands: natural multifonctionality and human undervaluation. Translated from French original version. HDR, Vol. 3, University of Paris 7, 266p.

Tchindjang, M, (2013) Mapping of natural hazards in Cameroon. International Cartographic Association. URL: https://icaci.org/files/documents/ICC.../403_proceeding.pdf

Tofani, V, Segoni, S, Agostini, A, Catani, F, and Casagli, N (2013) Technical Note: Use of remote sensing for landslide studies in Europe. Nat. Hazards Earth Syst. Sci., 13:299–309.

United Nation Office for Disaster Risk Reduction –UNISDR (2017) UNISDR'S contribution to science and technology for disaster rick reduction and the role of the international consortium on landslides (ICL). In: Sassa, K et al. (eds.), Advancing Culture of Living with Landslides, pp.109-115

USGS (2004) Landslides types and processes. 4 p. URL: https://pubs.usgs.gov/fs/2004/3072/pdf/fs2004-3072.pdf

Van Westen, CJ, Seijmonsbergen, AC and Mantovani, F (1999) Comparing landslide hazard maps. Natural hazards: J. of the Intern. Soc. for the Prev. and Mitig. of Nat. Hazards., 20:2-3, 137-158.

Varnes, DJ (1984) Landslide Hazard Zonation—A Review of Principles and Practice. IAEG – United Nations Scientific and Cultural Organization, Commission on Landslides, pp. 1-6.

Wang, L, and Qu, J. (2007) NMDI: A normalized multi-band drought index for monitoring soil and vegetation moisture with satellite remote sensing. Geophys. Res. Lett., 34, L20405.

Wang, H and Sassa, K (2005) Comparative evaluation of landslide susceptibility in Minamata area, Japan. Environ Geol., 47:956–966.

Wokwenmendam Nguet, P (2019) Petrography, geochemistry and geochronology of Nana complex (Tikar plain): geodynamic and metallogenic implications. Translated from French original version. PhD dissertation, Earth Sciences department, university of Yaoundé, Cameroon, 243p.

World Landslide Forum-WLF (2017) Advancing culture of living with landslides, pp. 109-115.

Wu, Y, Li, W, Liu, P, Bai, H, Wang, Q, He, J, Liu, Y, and Suns (2016) Application of analytic hierarchy process model for landslide susceptibility mapping in the Gangu country, Gangu province. Environ Earth Sci, 75:422.

Xiong, K, Adhikari, BR, Stamatopoulos, CA, Zhan, Y, Wu, S, Dong, Z, and Di, B (2020) Comparison of Different Machine Learning Methods for Debris Flow Susceptibility Mapping: A Case Study in the Sichuan Province, China. Remote Sens., 12:295.

Zhao, C and Lu, Z (2018) Remote sensing of landslides – A review. Remote Sens., 10:2, 279.

Appendix 1. ***Regression of MNMDI and Hydrothermal principal components bands***

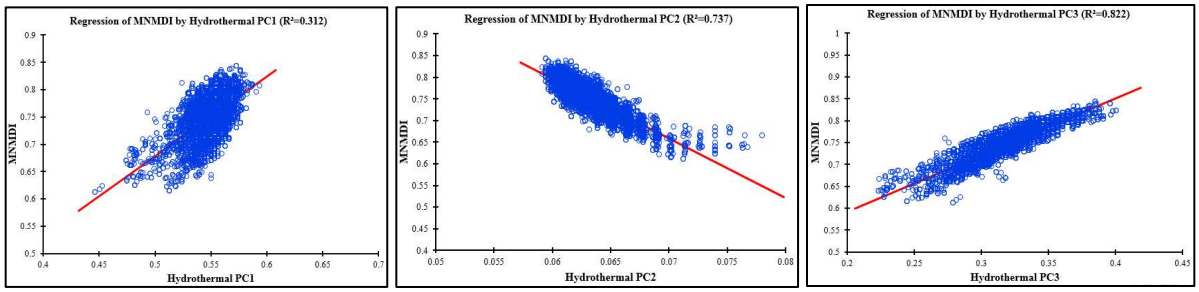

Appendix 2. ***Rainfall data for 1948-2018 (Green) and 2019 (Orange)***

	Zone 1		**Zone 2**		**Zone 3**		**Zone 4**		**Zone 5**		**Zone 6**		**Zone 7**		**Zone 8**		**Zone 9**		**Zone 10**	
	R	***D***	***R***	***D***	***R***	***D***	***R***	***D***	***R***	***D***	***R***	***D***	***R***	***D***	***R***	***D***	***R***	***D***	***R***	***D***
Jun.	350	27	350	25	352	28	352	25	369	25	361	25	377	25	389	24	358	26	369	27
Jul.	550	24	555	26	554	24	577	24	609	26	587	25	618	27	573	26	590	25	612	25
Aug.	617	25	620	25	648	25	650	26	654	28	658	28	688	29	687	31	679	30	692	27
Sept.	592	28	600	28	590	26	611	28	625	28	600	28	589	29	644	29	666	30	617	30
Oct.	378	26	377	26	392	23	379	25	391	24	398	24	395	23	412	23	445	25	400	24
Jun.	363	24	360	24	355	24	360	26	355	24	358	25	377	25	374	25	370	24	370	24
Jul.	546	25	583	25	535	24	579	24	579	26	600	26	557	27	548	28	571	25	577	25
Aug.	613	28	615	28	630	28	642	28	637	29	641	29	688	30	669	30	643	29	690	29
Sept.	597	30	580	28	581	28	594	28	618	30	617	30	615	29	644	29	621	30	633	29
Oct.	372	24	379	20	381	20	377	19	374	19	377	20	395	20	393	21	392	21	404	24

R=rainfall in millimeters and D=rainy days.

Figures

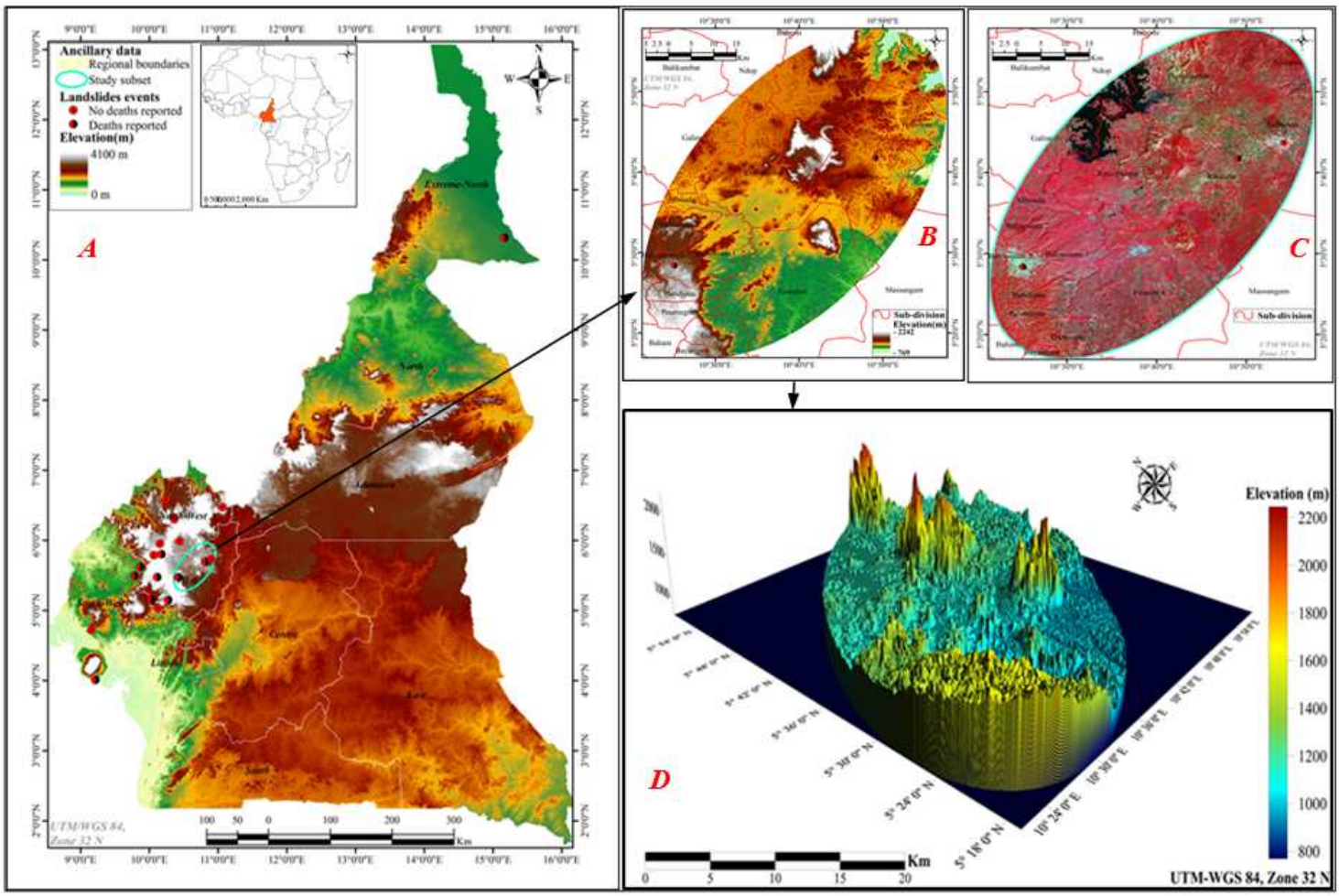

Figure 1

A) Country elevation and landslides events. B) & C) – Subset of study elevation and Landsat OLI-TIRS image. D) 3-dimensional appraisal of the subset elevation.

Figure 3

Scarps leaved by the landslides of Foumban (2018-A) and Bafoussam (2019-B). Both events were sudden with transitional to rotational movements, but the one in Foumban happened in one-step, while the one in Bafoussam happened during at least two steps (yellow dashed), justifying three main blocks/stairs.

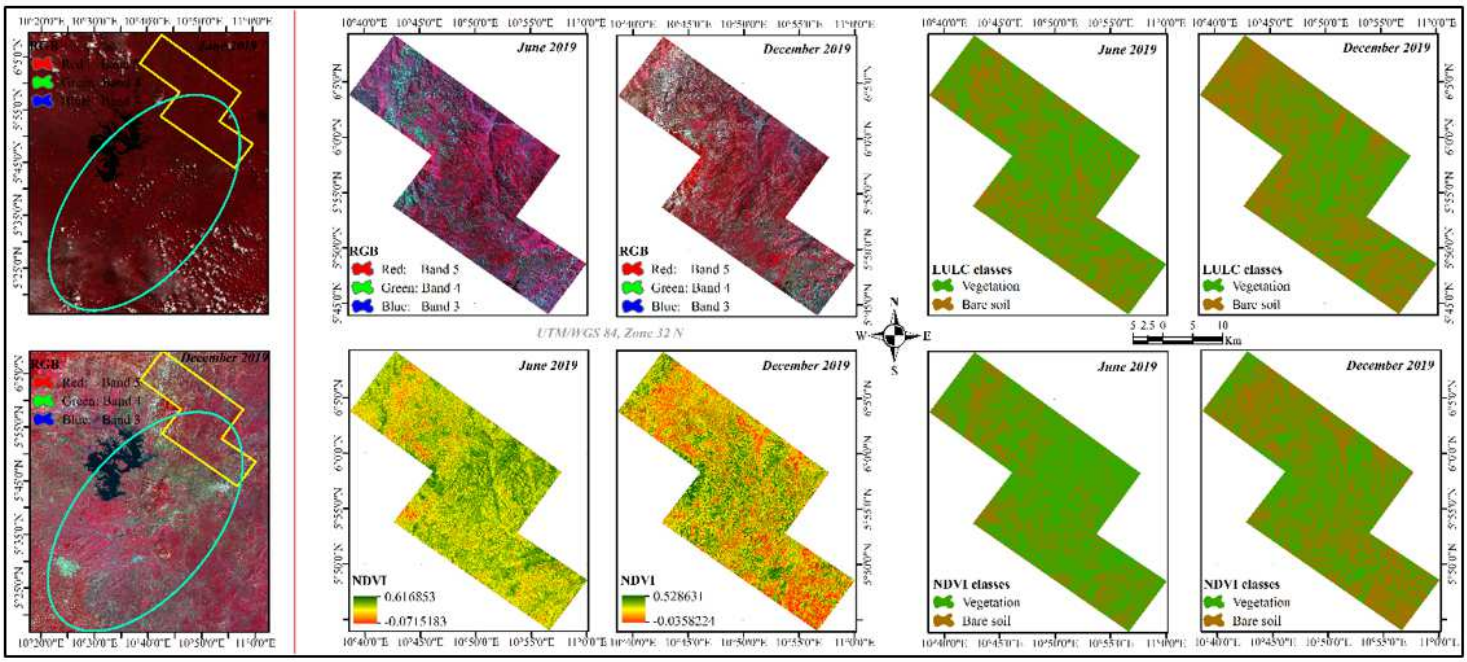

Figure 5

Subset of Landsat 8 images used for Land cover extent approximation

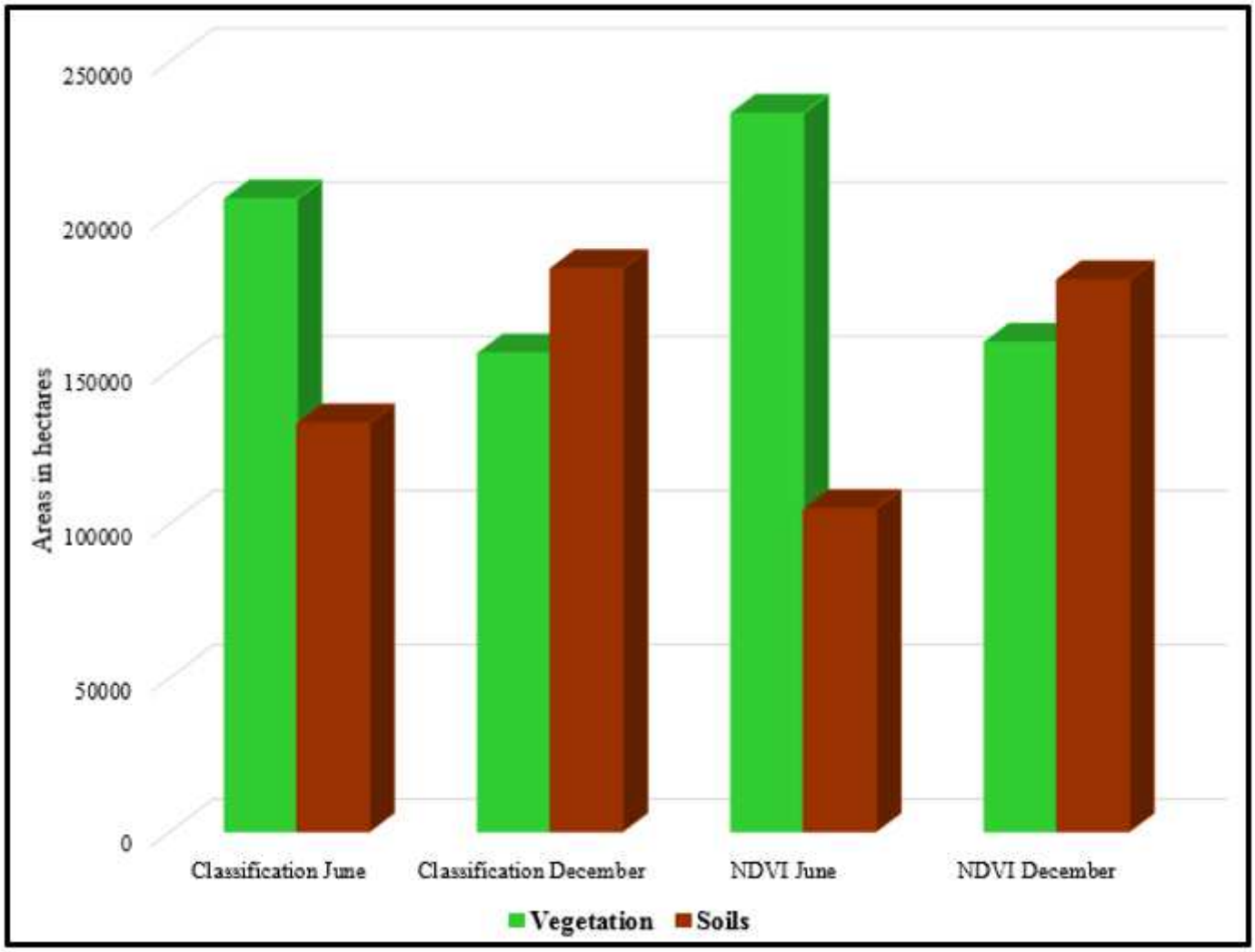

Figure 7

Land Use Land Cover (LULC) – comparison for the classification and the NDVI

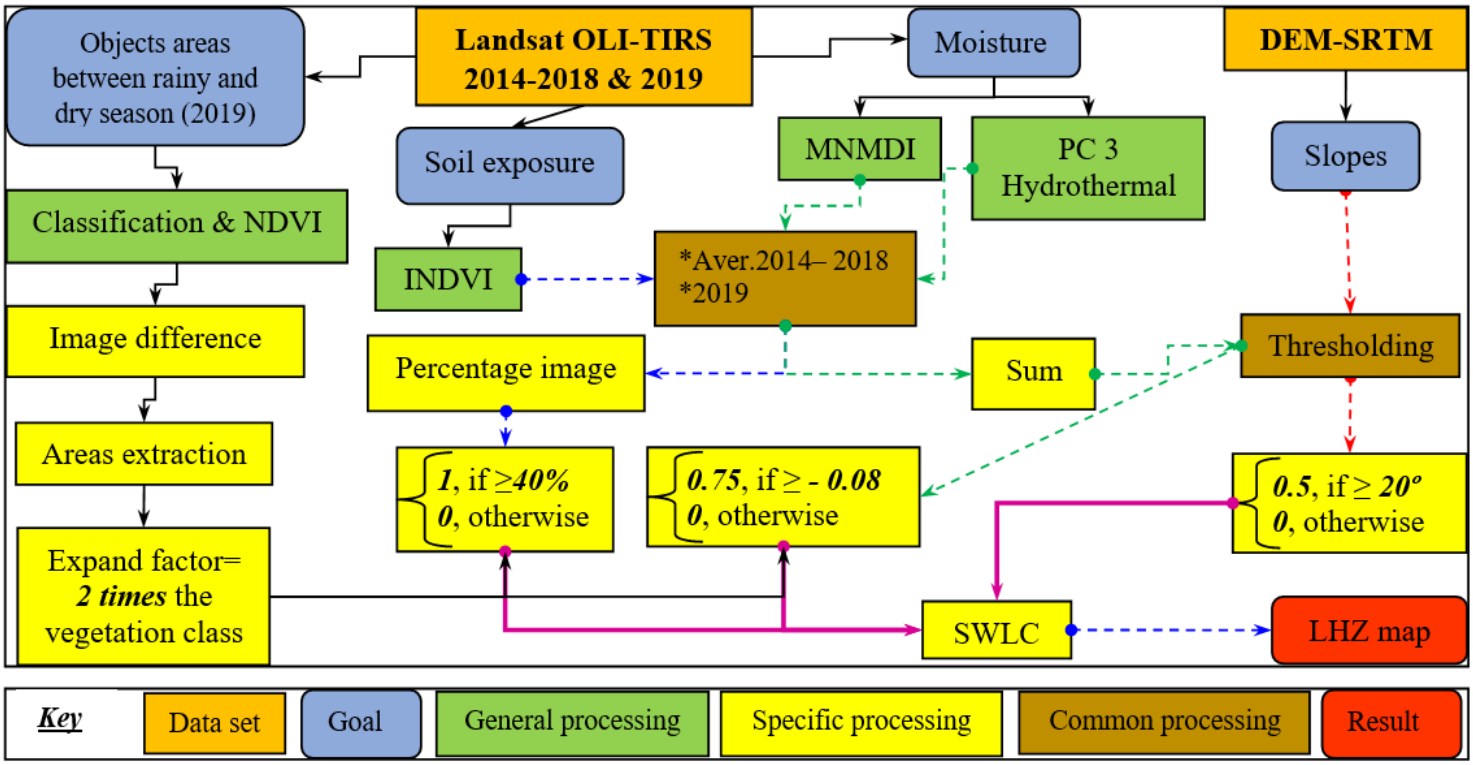

Figure 9

Workflow of the SLIP process

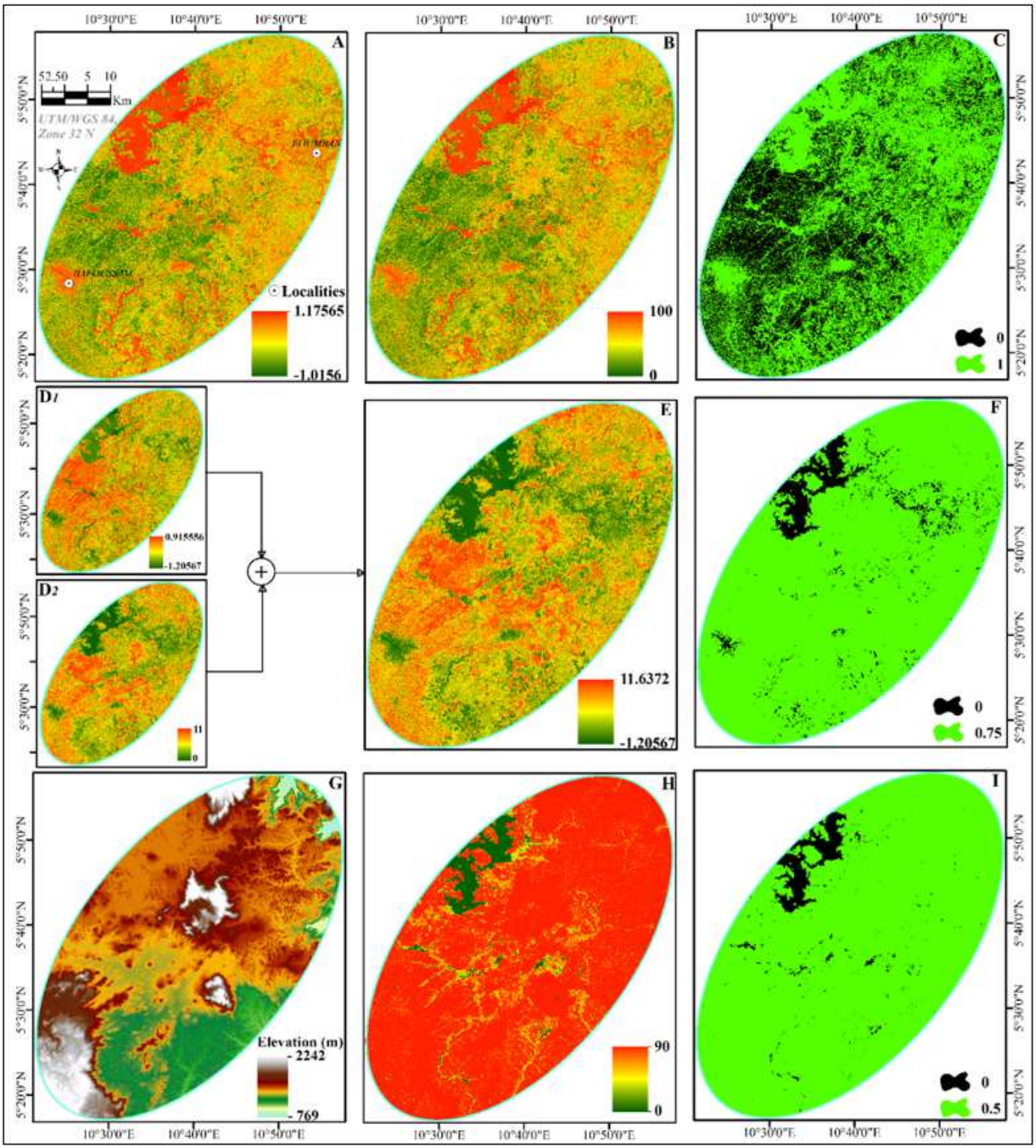

Figure 11

SLIP stretched and conditioned layers. A) INDVI stretched values; B) Barren land binned map; C) MNMDI + hydrothermal stretched map; D) Land moisture binned map; E-Slopes in degrees; F-Slopes binned map. Only remains the triggering factor identified as a long and huge rainfall condition. The DRIP algorithm helps assessing it.

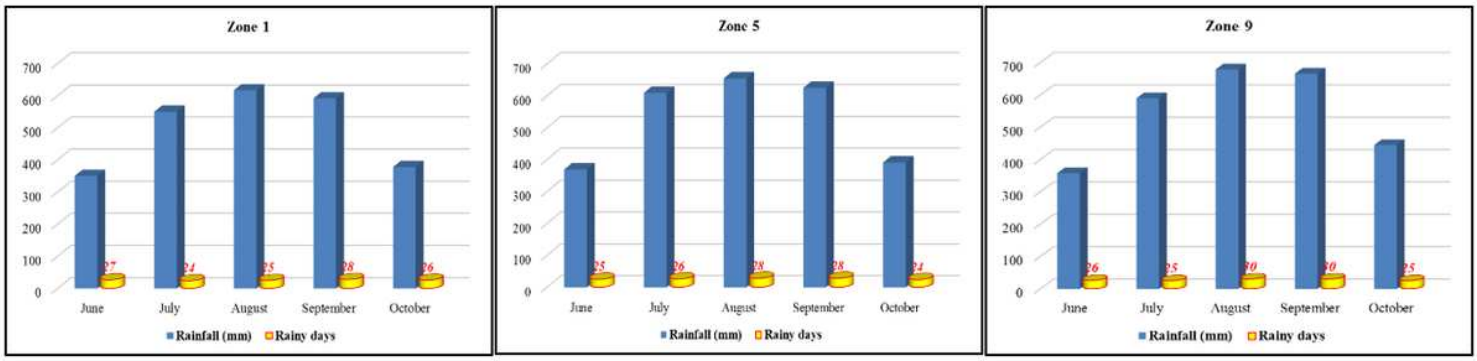

Figure 13

Monthly rainfall and rainy days sampled for three zones of the study area in 2019

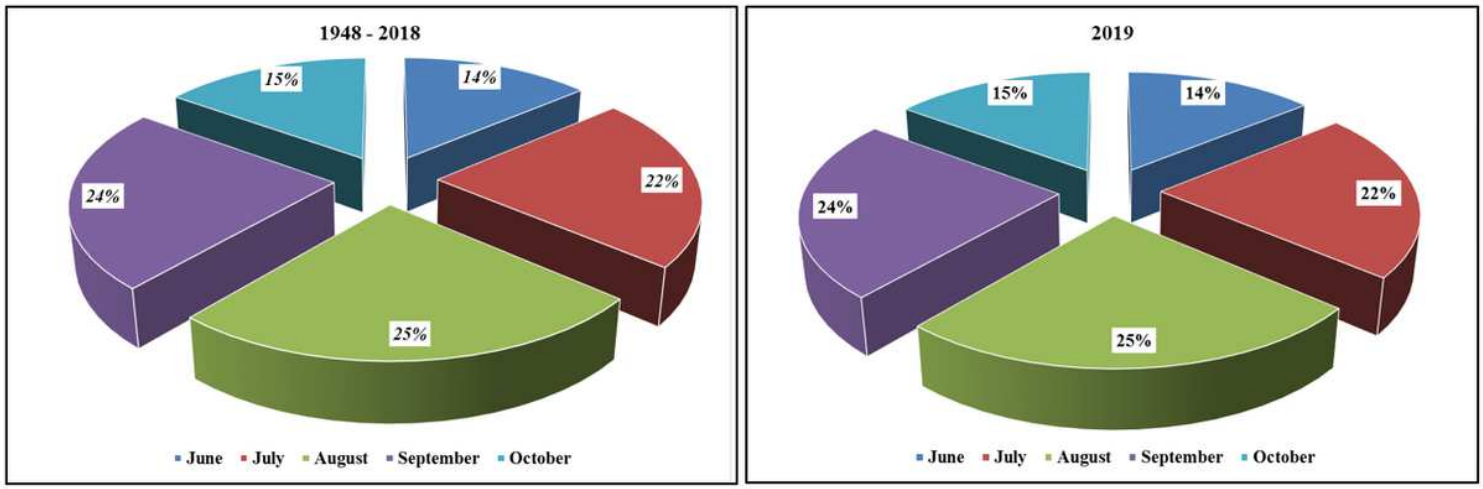

Figure 15

Percentages of monthly rainfall For June-October period

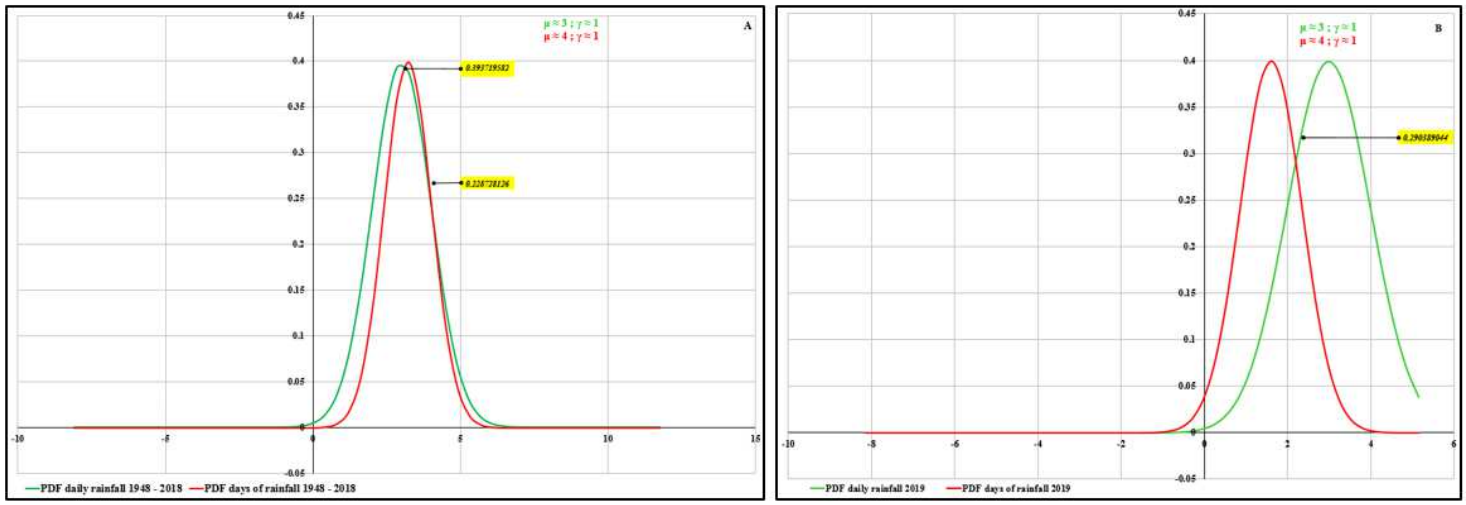

Figure 17

Individual PDF curves and their intersections before (A) and in (B) 2019

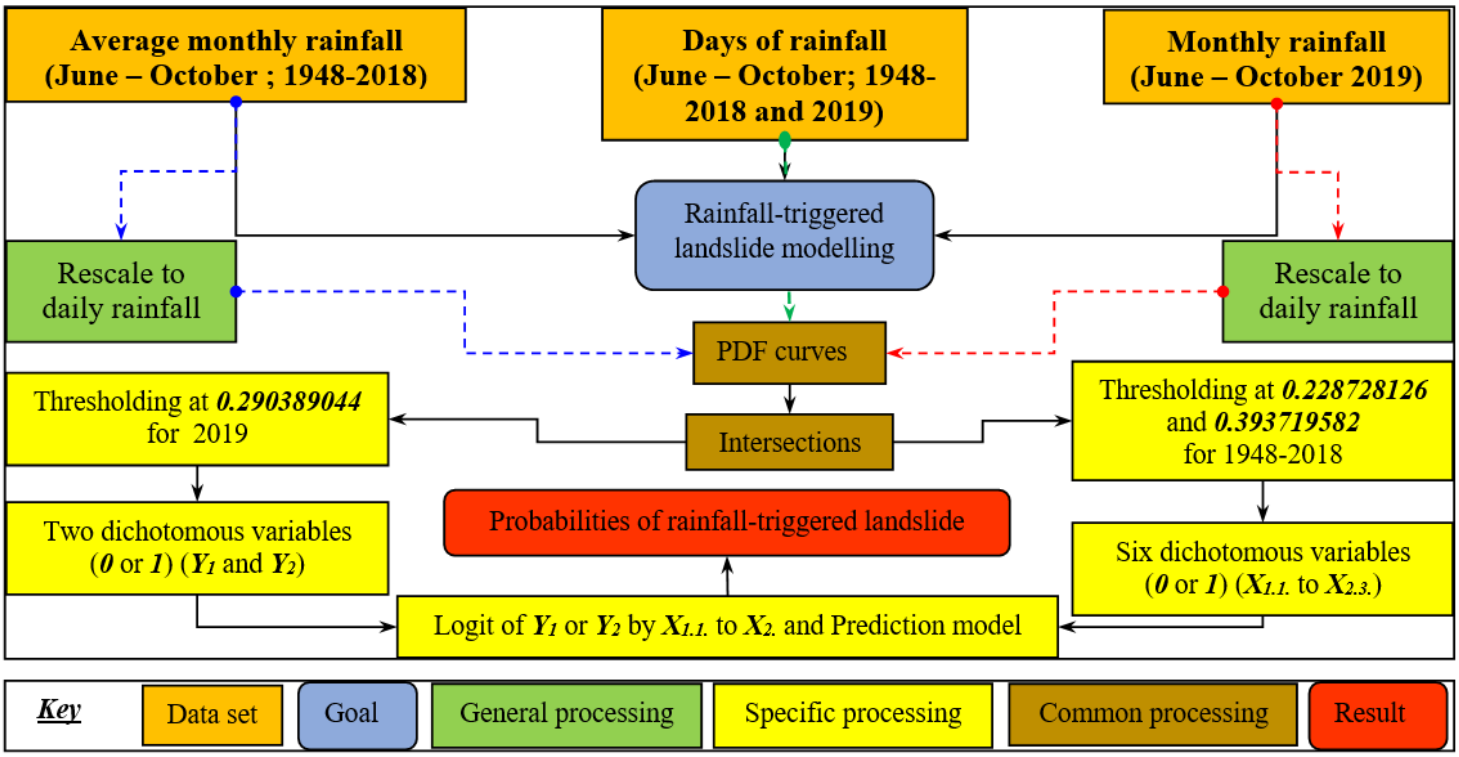

Figure 19

Workflow of the DRIP process

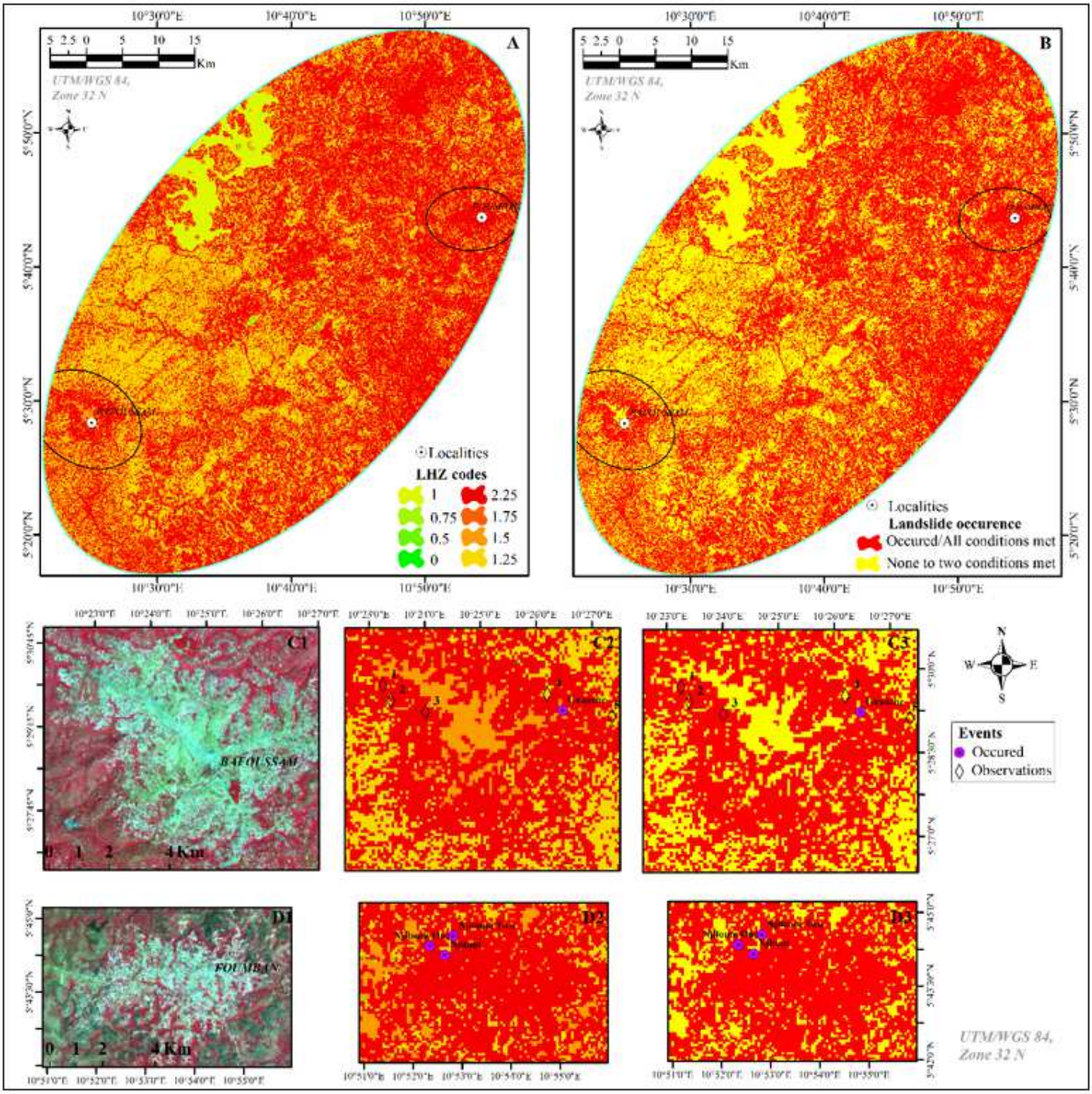

Figure 21

LHZ mapping. A) The eight classes and codes. B) Class 2.25 versus the other classes. C1) to C3) Patterns and accuracy assessment in Bafoussam. D1) to D3) Patterns and accuracy assessment in Foumban

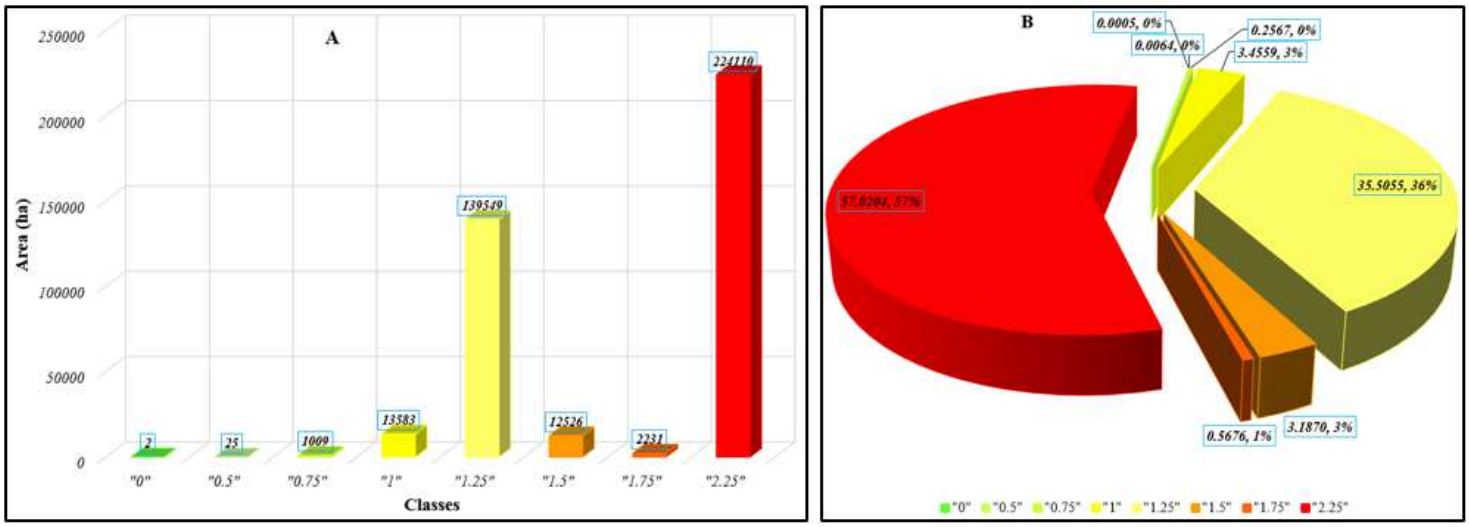

Figure 23

Areas (A) and percentages (B) of LHZ per classes

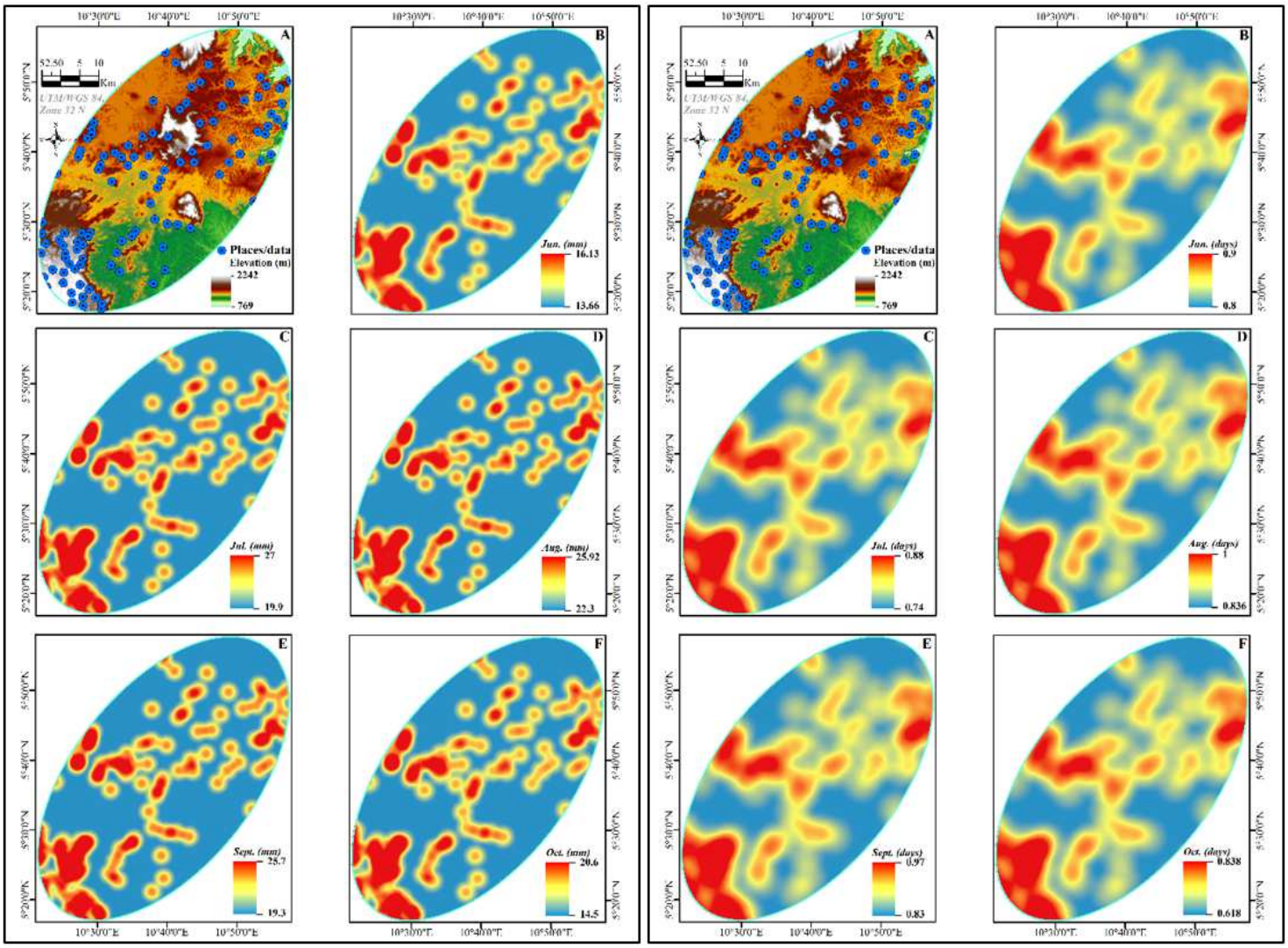

Figure 25

Daily rainfall (left) and days of rainfall (right) spatial distribution

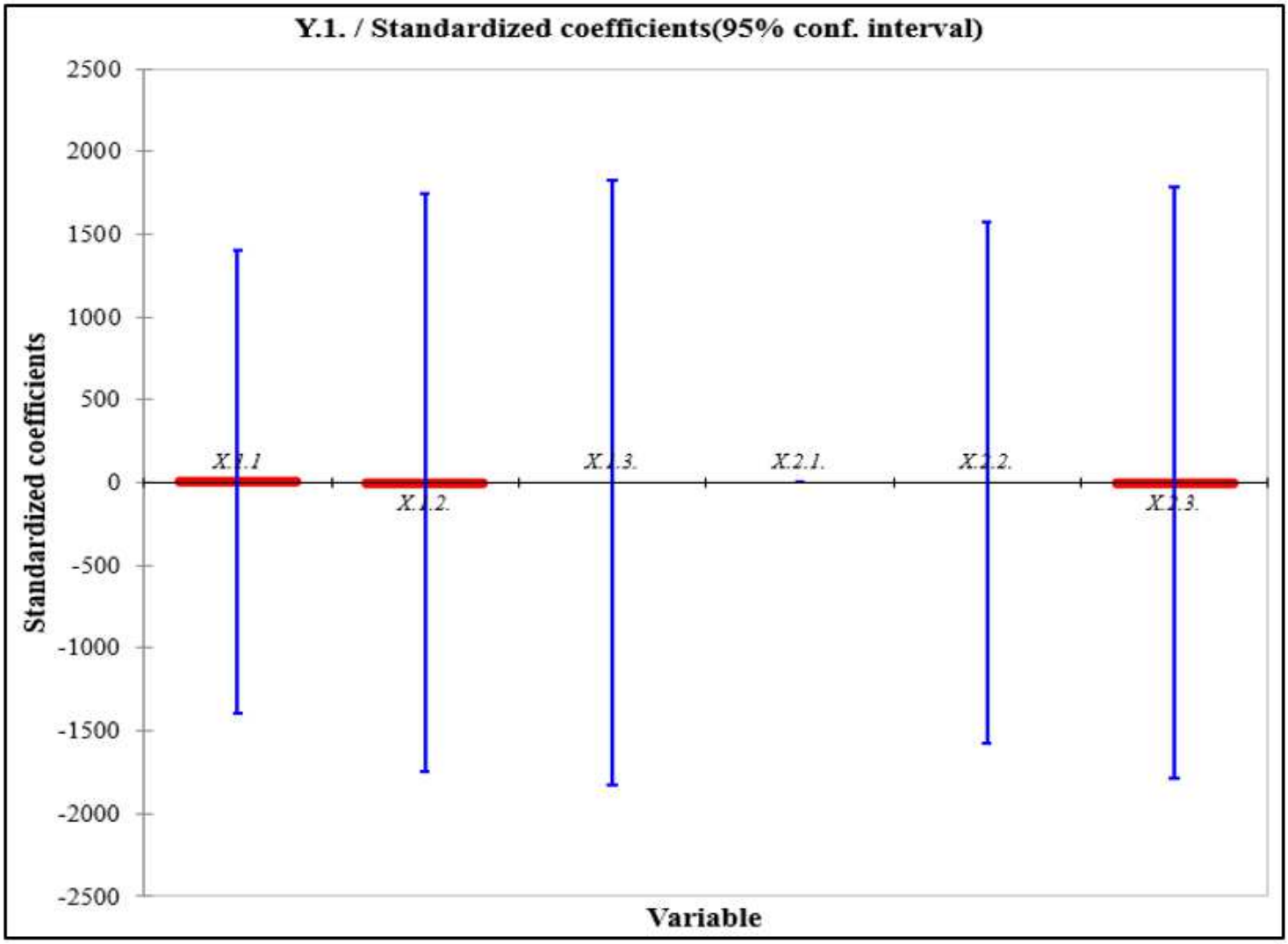

Figure 27

The standardized coefficients of the explanatory variables

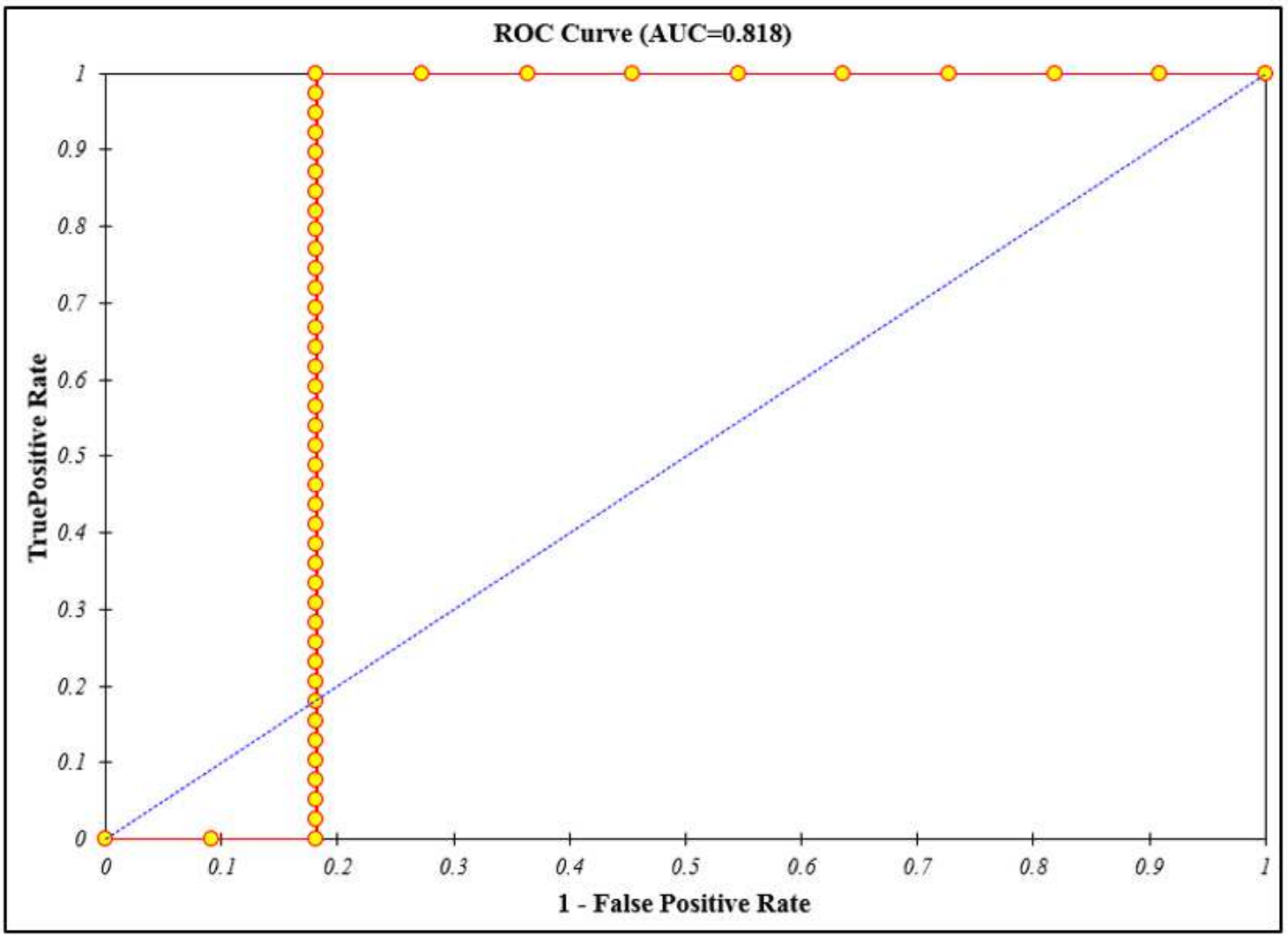

Figure 29

The Receiver Operating Curve of the model

Supplementary Files

This is a list of supplementary files associated with this preprint. Click to download.

- Appendix.docx
- Appendix.docx